Journal of Structural Geology 173 (2023) 104915

Contents lists available at ScienceDirect

Journal of Structural Geology

journal homepage: www.elsevier.com/locate/jsg

Fracture-pattern growth in the deep, chemically reactive subsurface

J.N. Hooker [a,*], R.F. Katz [b], S.E. Laubach [c], J. Cartwright [b], P. Eichhubl [c], E. Ukar [c], D. Bloomfield [d], T. Engelder [d]

[a] School of Mathematics, Science, and Engineering, University of the Incarnate Word, 4301 Broadway, San Antonio, TX, 78209, USA
[b] Department of Earth Sciences, University of Oxford, South Parks Road, Oxford, OX1 3AN, UK
[c] Bureau of Economic Geology, The University of Texas at Austin, 10100 Burnet Road Bldg. 130, Austin, TX, 78757, USA
[d] Department of Geosciences, Penn State University, 503 Deike Bldg., University Park, PA, 16802, USA

A B S T R A C T

Arrays of natural opening-mode fractures show systematic patterns in size and spatial arrangement. The controls on these factors are enigmatic, but in many cases the depth of formation appears to be critical. Physical, potentially depth-dependent factors that could account for these variations include confining stress, fluid pressure, and strain rate; these factors are common inputs to existing fracture models. However, temperature-dependent chemical processes likely exert an equally important control on patterns, and such processes have not yet been rigorously incorporated into models of fracture formation. Here we present a spring-lattice model that simulates fracturing in extending sedimentary rock beds, while explicitly accounting for cementation during opening of fractures, and for rock failure via both elastic and time-dependent failure criteria. Results illustrate three distinct fracturing behaviors having documented natural analogs, which we here term *fracture facies*. "Exclusionary macrofracturing" occurs at shallow levels and produces large, widely spaced, uncemented fractures; "multi-scale fracturing" occurs at moderate depth and produces partially cemented fractures having a wide range of sizes and spacings; and "penetrative microfracturing" occurs at great depth and produces myriad narrow, sealed fractures that are closely and regularly spaced. The effect of depth is primarily to accelerate both dissolution and precipitation reactions via increased temperature and porewater salinity; the specific depth range of each fracture facies will vary by host-rock lithology, grain size, strain rate, and thermal history.

1. Introduction

Natural fracture growth and pattern-evolution in the Earth is affected by the physical and chemical environment (e.g., Pollard and Aydin, 1988; Eichhubl, 2004; Laubach et al., 2019). Previous conceptual and numerical modeling work has mostly focused on the physical environment, treating rocks as elastic bodies that fail in response to applied loads—see especially the pioneering work on fracture spacing in bedded rocks (Price, 1966; Hobbs, 1967). This approach successfully explained the often-observed positive correlation between stratabound fracture spacing and layer thickness (e.g., Ladeira and Price, 1981) by showing that a tension applied remotely becomes zero at traction-free fracture walls, suppressing the development of fractures that are within some distance proportional to the height of the fracture-hosting layer (Ji and Suwatari, 1998; Bai and Pollard, 2001; Schöpfer et al., 2011), in beds having meter-scale or smaller thickness (Ladeira and Price, 1981; Chemenda et al., 2021).

Such models of layer-bound fractures in elastic media do not account for the wide fractures found in some deep wells (e.g., Olson et al., 2009), or the irregularly spaced to clustered fractures found in some outcrops (e.g., de Joussineau and Petit, 2021) and revealed in the subsurface by horizontal drilling (e.g., Li et al., 2018). A major advancement in this regard was to incorporate subcritical crack propagation in numerical models (Olson, 1993). In subcritical fracture growth, corrosive reactions in the high-tension region near fracture tips cause fractures to lengthen at stress intensities lower than those otherwise required to cause fracture growth (Atkinson, 1984). By incorporating this aspect of the chemical environment, more-realistic geological fracture patterns could be simulated numerically, supporting the importance of subcritical propagation and deepening our understanding of fracture interaction and clustering (Olson, 1993, 2004; Savalli and Engelder, 2005).

Advances in microstructural imaging of cemented and partially cemented opening-mode fractures containing characteristic crack-seal cement textures (Ramsay, 1980; Bons et al., 2012) indicate that fracture growth and porosity partitioning are controlled in part by synkinematic (during-opening) fracture cementation (e.g., Laubach et al., 2004a). Based on size-dependent porosity preservation, whereby sparse, large, partially open fractures are present amid abundant, fully cemented microfractures, Hooker et al. (2012) suggested that the primary mechanical effect of cement on fracture pattern evolution is to restore adhesion across fractures. This happens where cement deposition is fast enough to span the distance across fracture walls during fracture

* Corresponding author.
E-mail address: jnhooker@uiwtx.edu (J.N. Hooker).

https://doi.org/10.1016/j.jsg.2023.104915
Received 30 December 2022; Received in revised form 6 July 2023; Accepted 8 July 2023
Available online 11 July 2023

opening, a quality called *spanning potential* (Lander and Laubach, 2015). Where the variably sized fractures in a growing population have consequently variable spanning potential, more completely cemented (and small) fractures will be less likely to grow larger, compared to lightly cemented (and large) fractures. Thus a positive feedback loop emerges between fracture size and propensity to grow larger, leading to a power-law fracture size distribution (Hooker et al., 2012).

With a solid cement bond spanning the intermittently disconnected fracture walls, tension can then be transmitted across the fracture, in violation of the original fracture-spacing models cited above (e.g., Price, 1966) that assume fractures, once opened, are acted upon only by fluid pressures. In the past decade, advances in numerical modeling have enabled exploration of several consequences of fracture cementation. Virgo et al. (2014) showed how the style of fracture reactivation, including deflection and crosscutting, depends on the relative strength of the cement and the host rock, as well as any rotation of the stress field. Vass et al. (2014) came to a similar conclusion about the importance of cement strength, and showed that cementation dynamically affects the porosity and permeability evolution of fractured layers. Hooker and Katz (2015) simulated the adhesive effects of cementation within fractures in a spring-lattice numerical model; they showed how cementation rates that are fast, relative to layer-extension rates, produce smaller and more closely spaced fractures.

Moreover, cement accumulation within intergranular porosity in the host rock contributes to mechanical stiffening (Laubach et al., 2009), and cementation of bedding planes can suppress sliding, a mechanism proposed to halt fracture propagation and thus achieve layerbound fracturing (Price, 1966; Schöpfer et al., 2011). Thus the effects of the chemical environment on fracture pattern development are diverse, and can potentially explain enigmatic fracture-pattern characteristics such as power-law size distributions (Clark et al., 1995; Hooker et al., 2014; Späth et al., 2022) and spatial clustering that is statistically distinguishable from both periodic and random arrangements (Gillespie, 2003; Hooker et al., 2018, 2023; Marrett et al., 2018; Bistacchi et al., 2020; Corrêa et al., 2022). However, to date the two distinct chemical effects mentioned above—chemically-assisted crack growth and synkinematic sealing—have not been incorporated into a model that can examine their effects independently and in combination.

This study aims to establish that the depth of fracture formation affects the resulting patterns, not only through the well-established physical mechanisms of overburden and confining stress, but also through thermally controlled chemical mechanisms of cementation and chemically-assisted fracture growth. A fundamental assumption is that both precipitation and dissolution reactions are promoted through enhanced kinetic rates at higher temperatures (e.g., Meredith and Atkinson, 1985; Lander et al., 2008; Ankit et al., 2015). Here we support this view using new data from natural fractures and numerical modeling. In the following section, we present new fracture data from three separate geologic settings that illustrate the importance of thermally accelerated synkinematic cementation and chemically assisted, subcritical fracture growth on fracture pattern evolution. Next, to illustrate a simplified example of fracture pattern growth wherein these processes dominate, we extend a spring-lattice numerical model of fracture opening in response to layer-parallel extension (Hooker and Katz, 2015) to combine synkinematic cementation with a time-dependent, subcritical failure criterion. Finally, we identify parallels between model output and natural patterns, schematizing several categories of model results as *fracture facies*, which in part provides a mechanistic basis to the oft-observed link between fracture patterns and sedimentary facies (e.g., Bruna et al., 2015).

2. Natural examples of pattern attributes varying with fracture cement

2.1. Contrasting size distributions, structural styles, and spanning potentials: an example from the Scottish Highlands

Natural opening-mode fracture arrays in sedimentary rocks worldwide have size distributions that vary by cement content: arrays containing abundant synkinematic cement are present in power-law aperture-size distributions, i.e.:

$$w = aN^{-b} \tag{1}$$

where w is fracture kinematic aperture, meaning total distance between fracture walls (Marrett et al., 1999), N is cumulative number (1 for the largest aperture, 2 for the second-largest, and so on) and a and b are constants. In contrast, barren or lightly cemented fractures commonly have narrow aperture-size ranges, often visible in outcrop. These trends have been documented for sandstones (Hooker et al., 2009, 2014) and limestones (Ortega et al., 2010; Hooker et al., 2012).

To some extent, contrasting patterns in sandstones of what could be called "veins" and "joints"—referring to heavily and lightly cemented fractures, respectively—can be attributed to physical, rather than thermochemical, aspects of formation-depth. For example, Gillespie et al. (2001) interpreted that joints in the Burren limestones of Ireland had restricted fracture lengthening due to their shallow formation: low overburden stress on bedding planes allowed for slip along them, which halted joint propagation. Late joints also abut against earlier, but still uncemented, joints. The presence of these barriers to propagation produced a narrow range in fracture length, best fit by a lognormal distribution, and a correspondingly narrow aperture-size distribution (Gillespie et al., 2001). In contrast, veins formed at depth, where fractures were interpreted to have grown subcritically and barriers to propagation were not active; the result was a power-law length distribution and a wide aperture-size distribution (Gillespie et al., 2001). Here we describe an example from the Scottish Highlands, near Dundonnell (Fig. 1), which shows qualitatively similar populations of cemented and uncemented fractures hosted in sandstone. Crack-seal microstructures and crosscutting relationships, revealed in the field and using scanning electron microscope-based cathodoluminescence (SEM-CL), show that it is cementation that permits fracture crosscutting. Size distributions and structural styles are indeed strongly depth-dependent, but in this case, they owe as much to the chemical environment as to the physical.

Field exposures of the Cambrian Eriboll Group sandstones facilitate

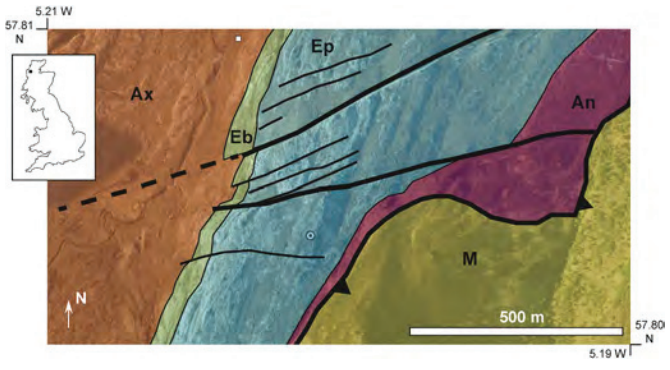

Fig. 1. Geologic setting of Dundonnell fracture arrays, NW Scottish Highlands. The town of Dundonnell lies approximately 4 km to the north. Sample location indicated by circle (see Fig. 2). M: Moine Supergroup (Neoproterozoic); Ax: Applecross Formation (Neoproterozoic); Eb: Eriboll Formation, Basal Quartzite member (Cambrian); Ep: Eriboll Formation, Piperock member (Cambrian); An: An-T-Sron Formation (Cambrian). Basemap photograph from Google Earth. Contacts and faults based on Peach et al. (1907), Laubach et al. (2014), and field observations from the present study.

fracture mapping upon rock faces polished and striated during Pleistocene glaciation (Krabbendam and Glasser, 2011). The outcrops we focus on are present meters away from the Moine Thrust Belt (Fig. 1), a regional suture zone reflecting Caledonian convergent tectonics (Trewin and Rollin, 2002). Regional offshore and onshore surveys demonstrate multiple distinct episodes of widespread faulting, including Devonian ENE-WSW extension and Permo-Triassic NW-SE extension (Wilson et al., 2010). Fission-track analysis has revealed a complex post-Caledonian structural history, with multiple burial-exhumation episodes (Holford et al., 2010). Consistent with these regional observations is the presence of multiple sets of cemented, opening-mode fractures having consistent crosscutting relationships (Laubach and Diaz-Tushman, 2009; Elmore et al., 2010).

Macrofractures, here defined as fractures sufficiently large to be seen without use of a microscope (> approximately 0.1 mm in aperture), are present as centimeters to tens of meters-long, planar, near vertical structures, containing little or no quartz cement (Fig. 2). We focus on a plan-view exposure of fractures (Fig. 2) so layer boundedness is not readily observable, but regional surveys (Laubach and Diaz-Tushman, 2009; Hooker et al., 2011) indicate that fractures range from hierarchical to unbounded, in the sense of Hooker et al. (2013). Fractures of various orientations tend to abut or branch rather than crosscut one another (Fig. 2). Where macrofractures are closely spaced they may coalesce into faults (Figs. 2 and 3), some of which are visible on aerial or satellite images (Fig. 1) and have meters to tens of meters of offset.

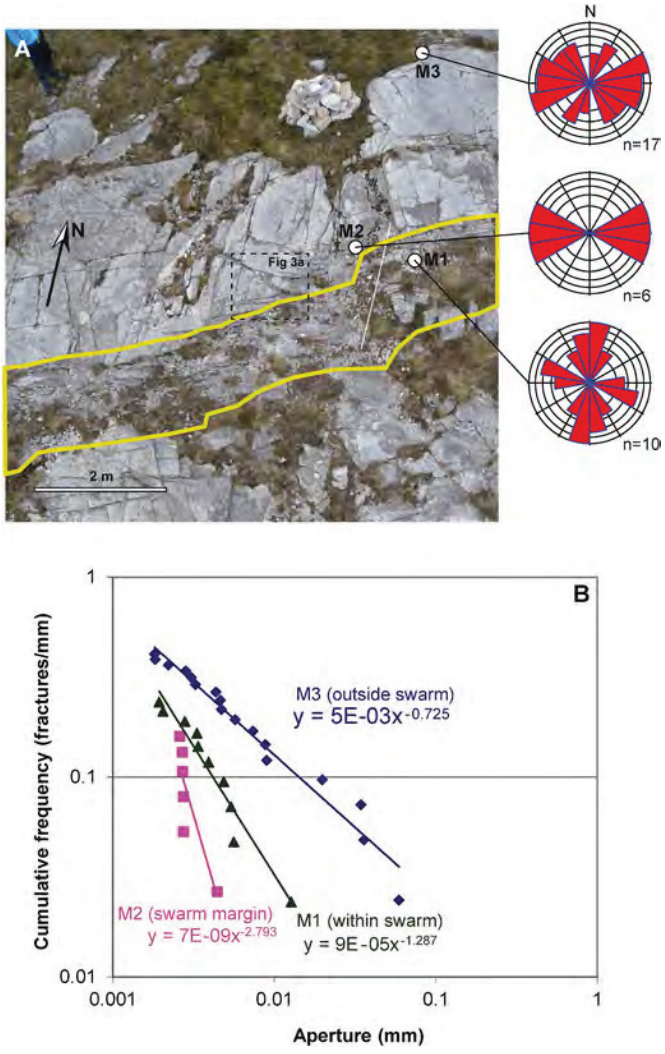

Fig. 2. (A) Macrofractures at Dundonnell outcrop. Highlighted in yellow is a segment of a macrofracture swarm, forming an incipient fault via linkage of uncemented opening-mode fractures. Locations of microfracture samples shown, with corresponding rose diagrams of microfracture strike. (B) Aperture-size cumulative frequency distribution of microfracture populations measured using SEM-CL in samples M1, M2, and M3. Note M3 has the greatest microfracture frequency and lies at greatest distance from macrofracture swarm. (For interpretation of the references to color in this figure legend, the reader is referred to the Web version of this article.)

Microfractures were observed using SEM-CL, which allows precise delineation of microfracture quartz cements in optical continuity with host-grain quartz (e.g., Laubach et al., 2004a, b). SEM-CL maps of microfractures illustrate systematic sets of quartz-filled microfractures based on subparallel strikes, crosscutting relationships, and CL color (Fig. 3c). Microfractures locally contain crack-seal texture and commonly crosscut one another, with little change in orientation near their intersections (Fig. 3c). We observed microfractures within three samples—M1, M2, and M3 (Fig. 2)—taken from within the macroscopic fault zone, at the margin of the fault zone, and outside the fault zone, respectively. We quantified microfracture frequency using 1D scanlines of observations, drawn upon layer-parallel thin sections. Along each scanline we recorded fracture kinematic aperture and position where each fracture intersects the scanline (e.g., Gillespie et al., 1993). We trigonometrically corrected fracture apertures and spacings. To each aperture size we assigned a cumulative number (Equation (1)), then divided that number by scanline length, giving the cumulative frequency for each aperture size. Plotting cumulative frequency versus aperture size (Fig. 2b) gives all the information of a size histogram without the need for selecting a bin size.

We also quantify fracture network properties from field and SEM-scale photomosaics (Fig. 3b, d) according to the *I-X-Y* method of Manzocchi (2002) and Sanderson et al. (2018). In this method, *I* nodes are defined as isolated fracture terminations. *Y* nodes form where three fracture segments meet, for example at a branching point or an abutment of one fracture against another. *X* nodes form where four segments meet, usually marking a crosscutting intersection. An *I-X-Y* ternary plot (Fig. 3e) accounts for a network's relative abundance of the three types of node. Differences in *I-X-Y* proportions are apparent between the macro scale, which is dominated by *Y* nodes, and the micro scale, which is dominated by *I* nodes, with subsidiary *X* nodes outnumbering *Y* nodes (Fig. 3e, Table 1).

Interpretation. The microfractures and macrofractures we observed in the Eriboll sandstone are likely not genetically related, based on a lack of correspondence in strike (Fig. 2) and degree of cement infill. Furthermore, if microfractures and macrofractures formed together, then we might expect microfracture frequency to systematically increase near the macroscopic fault zone—or even to systematically decrease, if fault slip resulted in stress shadowing. Instead, we observe no consistent relationship between microfracture frequency and distance (Fig. 2). The salient difference between microfracture and macrofracture networks is that the latter are dominated by *Y* nodes, manifest as abutting intersections. We interpret that the macrofractures are younger, having formed after the microfractures were filled with cement. Macrofracture propagation was halted where fractures intersected pre-existing, uncemented fractures. Halting was enabled by sliding along the pre-existing fracture. Previous analysis suggests that during evolution of wing-crack arrays into faults, an opening-mode "parent" crack orientation is critical to promoting sliding, localization, and incipient fault slip (Myers and Aydin, 2004).

In contrast, microfractures commonly form *X* nodes where they intersect, meaning they crosscut rather than abut. Distinct CL response of microfracture cement implies distinct generations, where previous fractures opened and sealed before later generations of fractures form. This interpretation is consistent with multiple fracturing episodes throughout a protracted tectonic history in a rock prone to brittle deformation (Laubach and Diaz-Tushman, 2009; Holford et al., 2010; Hooker et al., 2011). Cementation precluded sliding on pre-existing microfractures, enabling continued propagation and the formation of

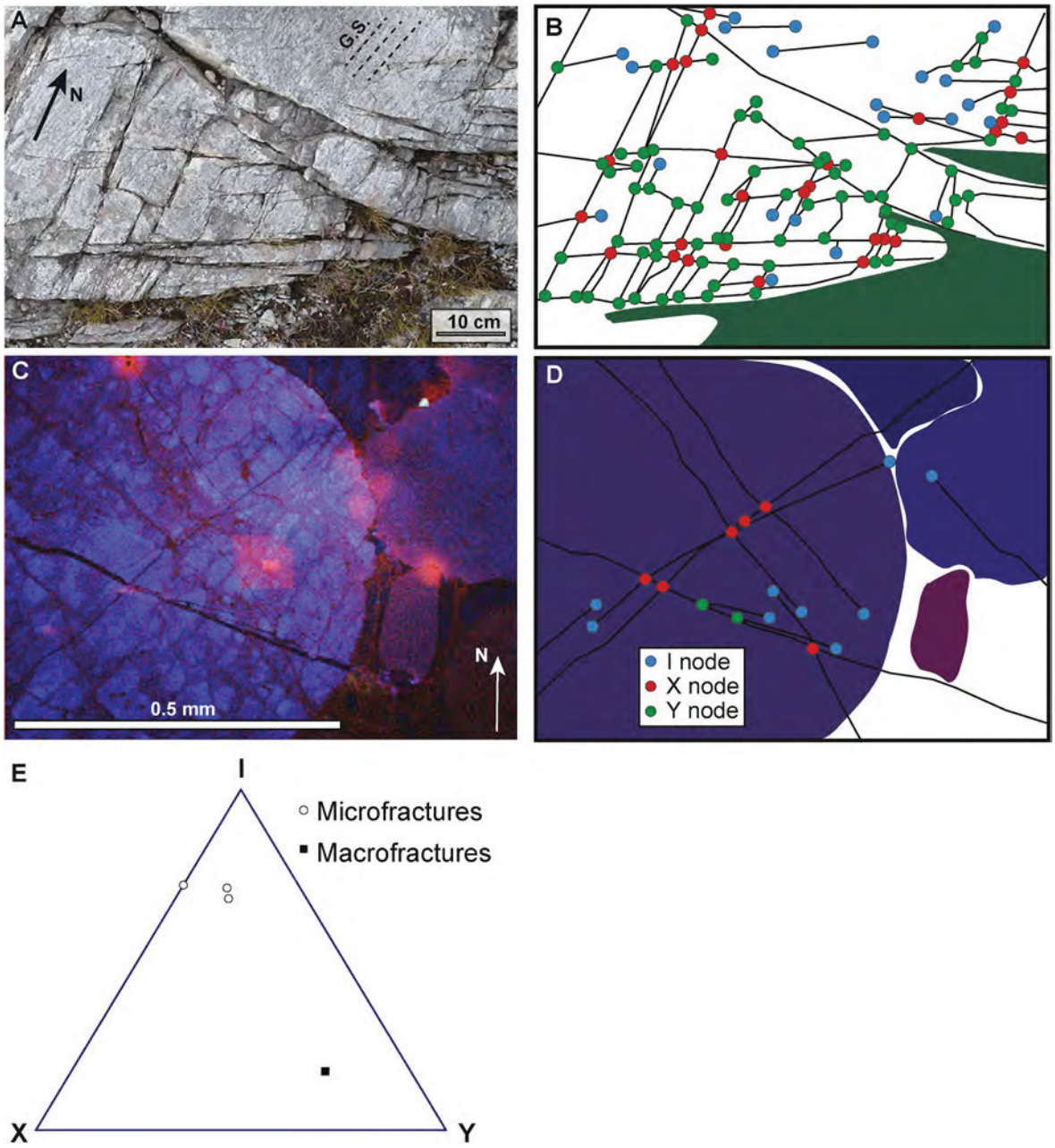

Fig. 3. (A) Detail of macrofracture array shown in Fig. 2, with fracture network nodes interpreted—see text. G.S.: glacial striations. (B) Interpretation of fractures and nodes in (A). (C) SEM-CL image of microfractures, sample M3 (Fig. 2). (D) Interpretation of fractures and nodes in (C). (E) Ternary plot showing frequencies of I, X, and Y nodes, from micro- and macrofracture populations in Fig. 2.

Table 1
I-X-Y data, Dundonnell outcrop (Scottish Highlands).

Sample	*I* nodes	*X* nodes	*Y* nodes
Outcrop macrofractures	73	88	262
M1	32	8	5
M2	18	7	0
M3	68	19	13

X nodes. Similar resistance to reactivation stemming from cementation was inferred from fracture patterns in the Flathead sandstone by Forstner and Laubach (2022).

2.2. Contrasting fracture-bedding relations: an example from the Appalachian basin

The previous example shows how the prevalence of abutting, rather than crosscutting, can drastically impact resulting fracture patterns. Abutting is favored where traction-free (barren), pre-existing fractures can accommodate the opening of a new intersecting fracture via sliding and formation of a *Y* node. Crosscutting, *X* nodes are favored where fractures are sealed and cannot slide. For the same reason—sliding—bedding planes may be equally important as pre-existing fractures in sedimentary rocks. Shales, in particular, are known for their mechanical anisotropy, imparted by weak bedding planes, which has been shown to affect fracture propagation in previous studies (e.g., Peacock and Sanderson, 1992; Gomez-Rivas and Griera, 2012; Lee et al., 2014; Hooker et al., 2020; Haluch et al., 2023). An example derived

from cores through the Marcellus Formation in the Appalachian basin shows how fracture orientations in folded, laminated rocks vary significantly by degree of cementation. Here again, fracture style reflects the combined effects of the physical and chemical environment of fracture formation.

Fractures were recovered from shallow (maximum true vertical depth 400 ft (120 m)) vertical core drilled through the Marcellus shale. Core was collected from a moderately (~30°) dipping forelimb in the Valley and Ridge province of the Appalachian basin in central Pennsylvania, USA (Fig. 4). The Appalachian basin includes a Paleozoic foreland basin sedimentary sequence that was folded into kilometer-scale anticlines with associated thrust faults during the Alleghanian orogeny (Faill, 1998). Structural style reflects both stratigraphic architecture and burial depth. Kilometer-scale folds were detached above Cambrian shales in the Valley and Ridge province, producing relatively tight fold geometries, compared to the broad anticlines within the Appalachian plateau to the northwest, where Silurian evaporites serve as the detachment (Mount, 2014). Areas of greater burial depth, such as in eastern Pennsylvania and southwestern Pennsylvania, western Maryland, and West Virginia, have relatively widely spaced thrust faults, compared to the study area in central Pennsylvania, where the maximum burial depth was shallower and the thrust faults are more closely spaced (Evans, 2023).

Regional fractures strike systematically parallel and perpendicular to fold axes (Srivastava and Engelder, 1990), with steeply dipping, fold-axis-oblique fractures present that pre- and post-date folds (Evans, 2010; Evans et al., 2014). Wilkins et al. (2014) noted that curvature of the thrust belt into the Pennsylvania salient could explain scatter in fracture orientation, and so favored a single, though protracted, brittle deformation event. Layer-parallel fractures are particularly abundant in organic-rich shales, including within the sampled Marcellus Formation, as detailed below. The broad distribution of layer-parallel fractures in the overlying shales of the Catskill Delta Complex, and in organic-rich shale layers throughout the Appalachian plateau in northwestern Pennsylvania and in New York (Engelder and Gross, 2018) has been interpreted to stem from organic maturation, low permeability, and mechanical properties of shales (Hooker et al., 2017a; Engelder and Gross, 2018).

Core for this study sampled the Marcellus shale (Middle Devonian). Most fractures are parallel or perpendicular to bedding, which dips about 30° to NNW. The database includes 496 total fractures, of which 54 show evidence of shear offset, in the form of slickensides, slickencrysts, or pressure-solution cleavage oblique to fracture walls. Opening-mode fractures have planar geometries and discrete, smooth walls (Fig. 5). Because of the limited fracture height preserved in core, fracture tips are not generally preserved; however, tips that are preserved indicate that fractures commonly abut against bedding planes. Owing to extensive core breakages, along fractures and bedding planes, fracture strike and dip were identified within ten-degree windows, and not more precisely.

Fractures are dominantly calcite cemented, with subsidiary quartz and pyrite. Fractures were grouped by degree of cementation according to the scheme shown in Table 2.

Group 0 fractures are dominantly bedding-perpendicular and strike NE, with subsidiary NW-striking counterparts (Fig. 6). Group 1 fractures show strike patterns similar to those of Group 0, but with more variation in dip. Although most Group 1, NE-striking fractures are bed-perpendicular, a considerable subset dips more shallowly to SE. These latter fractures are therefore oblique to bedding and to the horizon. Group 2 and 3 fractures are almost uniformly parallel or perpendicular to bedding, omitting fractures with evidence of shear displacement. Group 3 includes a population of bedding-parallel fractures, which are entirely filled with cement.

Interpretation. Group 3 fractures are thoroughly cemented, in some cases with fibrous cement, interpreted to form during fracture opening, based on kinematic models (Urai et al., 1991). The thorough cementation of Group 3 fractures is unlikely to have coincided closely in time with opening of Group 0 or 1 fractures, which contain no or little cement. A parsimonious interpretation is that Group 3 formed earliest, followed by Groups 2, 1, and 0, accounting for the paucity of cement as a

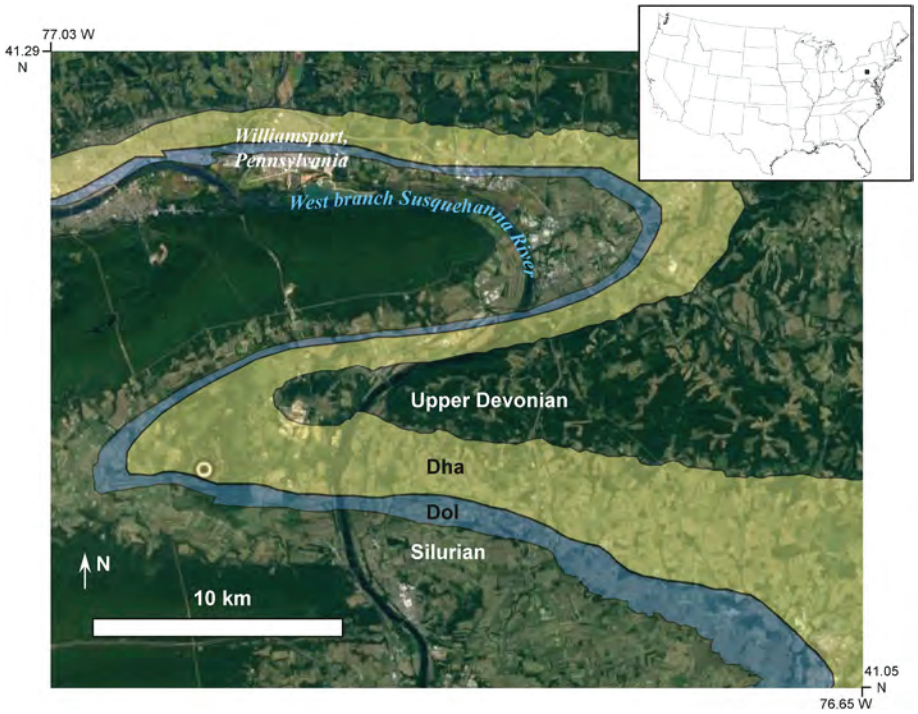

Fig. 4. Geologic setting for Appalachian basin core sample. Approximate core location shown (circle). Dha: Devonian Hamilton Group, the base of which is the Marcellus shale. Dol: Devonian Onondaga limestone. Silurian map area contains lower-most Devonian, the contact between which lies within the undivided Keyser and Tonoloway formations. Background photograph taken from Google Maps; geologic contacts modified after Berg et al. (1980).

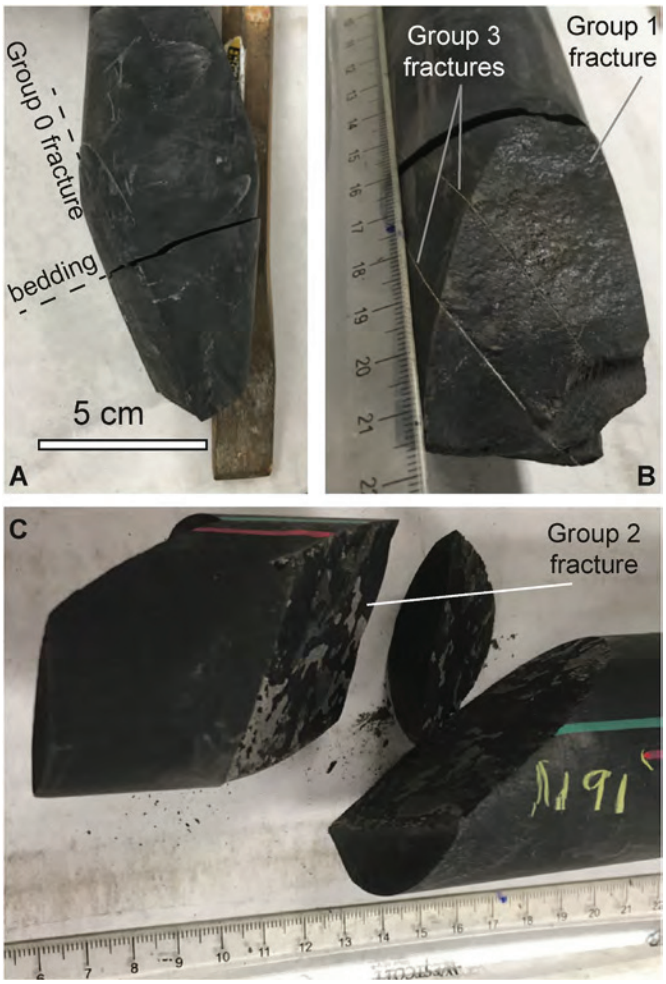

Fig. 5. Natural fractures recovered from State Game Lands 252 core. (A) Group 0 fracture, entirely lacking cement, depth 141 ft. Core has split along shale bedding plane. (B) Group 1 fracture, with thin, inconspicuous cement lining, cutting two Group 3 fractures, filled with white calcite cement. Depth 188 ft. (C) Group 2 fracture, with white but thin (<1 mm) cement lining, which is patchy rather than fully blanketing the fracture surface. Depth 191 ft.

Table 2
Categorization of opening-mode fractures based on fill, Appalachian basin.

Cement Group	Total N	Description
0	79	No evidence of cement
1	203	Walls continually or patchily covered by a patina of mineral cement, <0.1 mm thick, which has a translucent or sugary appearance
2	72	Walls continually or patchily covered by mineral cements that are locally thick enough to be opaque and white, but throughout <1 mm thick
3	92	Walls continually covered by opaque, white mineral cements; thicknesses commonly 1 mm or more

consequence of less thermal exposure as fracturing proceeded during exhumation. However, we have little direct evidence of relative timing in the form of crosscutting relationships. It may rather be that some fractures escaped mineralization as a consequence of gas generation, which may have driven off water, or by influx of undersaturated surface water, which may have diluted pore waters. We can conclude conservatively that the four fracture groups formed at distinct times.

The four fracture groups vary systematically in orientation, also suggesting a distinct time of formation for each group. We observe that the most heavily cemented fractures (Groups 2 and 3) are also arranged parallel and perpendicular to bedding, in contrast to lightly cemented fractures (Group 1), which lie oblique to bedding. Fractures can form at any time during the burial history of a sedimentary basin, even at very early, pre-lithification stages (Hooker et al., 2017b; Petit et al., 2022); nevertheless, fractures that strike parallel and perpendicular to map-scale folds, as well as layer-parallel fractures, are all anticipated to form during various phases of the evolution of fold-thrust belts (Ferrill et al., 2021). This evolution proceeds from a normal faulting stress regime during basin extension, to strike-slip and thrust-faulting with increasing horizontal tectonic load. Therefore the present fracture groups can all be interpreted in the context of Alleghanian tectonics. Furthermore, fluid inclusion studies have linked regional fractures to Alleghanian fold tightening and concomitant fluid-flow (Evans, 2010).

The opening-mode fractures that lie at high angle to bedding (Fig. 6) are kinematically coherent as pre- or early-syn-folding structures. For NE-striking fractures, a bed-perpendicular fracture will dip about 60° to SE. However, many NE-striking Group 1 fractures dip more shallowly to SE. If the dip were steeper, then a potential interpretation would be that these fractures formed subvertically, post-folding, and have not been rotated. Instead, their shallow dip would still restore to an oblique dip, even in restored bedding. This orientation is consistent with formation amid a thrust-faulting regime, such as the one that was present during Alleghanian folding (Engelder and Whitaker, 2006) or the one that persists today (Heidbach et al., 2018).

Interestingly, the attitude of uncemented Group 0 fractures is roughly perpendicular to bedding (Fig. 6). A potential explanation for this change in fracture orientation is that the Group 0 fractures formed at the shallowest levels, wherein the low burial stresses facilitated decoupling between strata, polarizing the stress field and driving the fractures in a more layer-perpendicular orientation, as is commonly observed for cross-joints linking pre-existing parent joints (e.g., Ji et al., 2021). If that explanation is true, then the oblique orientation, with respect to bedding, of Group 1 fractures is consistent with their formation under greater burial stress, which locked bedding planes and inhibited any such control of bedding on fracture orientation. This interpretation, though speculative, is also consistent with thicker cements accumulating on older fractures that formed deeper and under greater thermal exposure.

2.3. Variation in fracture intensity with depth: an example from the Piceance basin

The previous two examples show contrasting fracture patterns that also have varying spanning potentials. Those spanning potentials appear to have materially affected the resulting pattern, but in each case the protracted geologic history would have introduced other confounding variables, such as differential stress, strain rate, or fluid fluxes. To control for such variables, our final example focuses on fractures recovered from core at relatively great depth (2000–13,000 feet; 600–4000 m), from a basin with a comparatively simple burial history, and having a single predominant, regional fracture set. Therefore, we argue, variations in fracture pattern attributes—particularly fracture intensity—with depth can be attributed to depth-dependent variables like temperature, pressure, and perhaps fluid chemistry.

The Piceance basin (Fig. 7) is an intermontane sedimentary basin, whose sediments were deposited within the Cretaceous Western Interior Seaway that covered much of North America (Kauffman, 1984). The stratigraphic sequence contains gently folded, fluvial to marine sandstones and shales, and hosts a regional natural fracture set striking ENE, with subsidiary sets striking at high angle to this regional set (Lorenz and Finley, 1991). These fractures have garnered considerable attention for their effects on storage and flow of natural gas (Cumella and Scheevel, 2008). Combined burial history models and fluid inclusion studies support a basin-centered gas accumulation model for natural fracturing here (Fall et al., 2012), whereby maturation of coal beds at depth

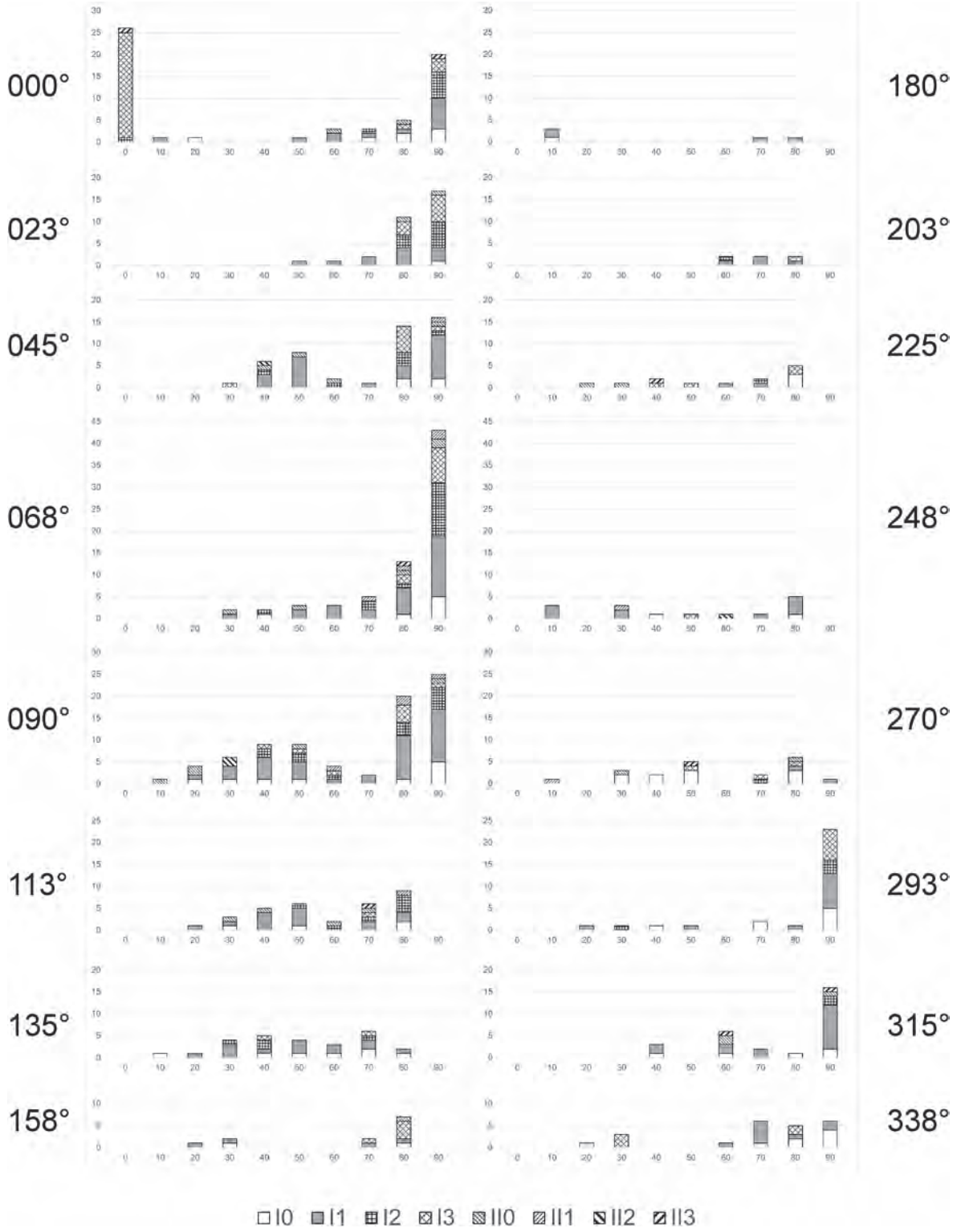

Fig. 6. Orientation of natural fractures recovered from Appalachian basin core. Orientations shown with bedding restored to horizontal. Azimuths (degrees) listed down either side represent the center of the strike window for the corresponding histogram. X-axis indicates maximum of dip window (degrees), with 0 indicating layer-parallel fractures. Symbol fill legend indicates kinematic mode (opening or shear) and cement group (Table 2). For example, "I0" means mode-1 (opening-mode) and Group 0; "II3" means mode-2 (shear-mode) and Group 3. Note moderately dipping fractures are dominated by opening-mode, Group 1 fractures—see especially fractures striking 045–135°.

resulted in fluid overpressures throughout the low-permeability sandstones above, eventually leading to fracture opening—as opposed to a conventional petroleum system in which gas accumulates in geometric traps, created by fractures or otherwise.

Here we focus on 47 core samples retrieved from fractured sandstones of the Mesaverde Group, from two distinct localities within the basin; namely, two clusters of oil fields in the north and south parts of the basin (Fig. 7). These two geographically distinct groups of samples

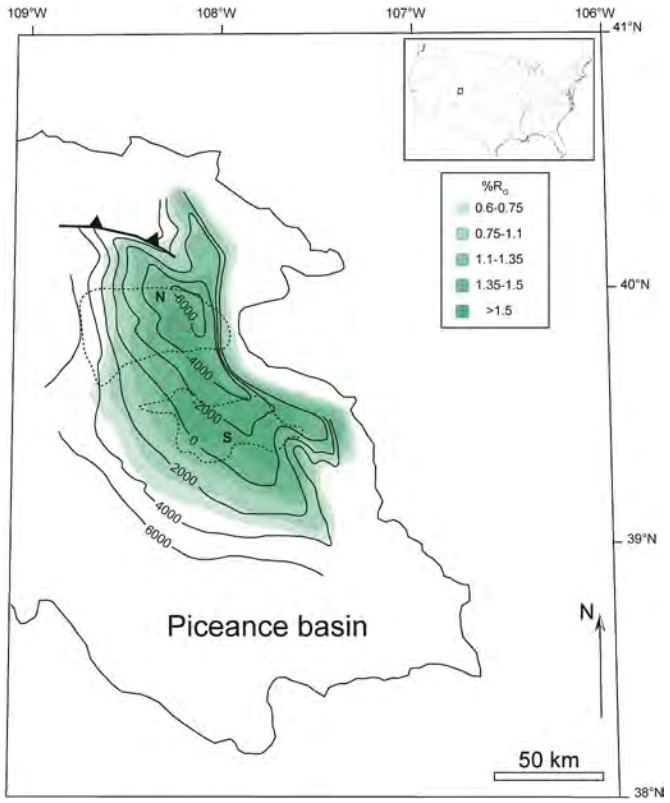

Fig. 7. Map of the Piceance basin. Solid contours show depths (in feet) to the top of the Rollins sandstone (after Cumella and Scheevel, 2008). Vitrinite reflectance maturity data from Nuccio and Roberts (2003). Dashed lines indicate fields from which north- and south- Piceance basin core samples were collected.

have undergone similar maximum thermal exposure, based on vitrinite reflectance (Nuccio and Roberts, 2003, Fig. 7). The southern sample suite (20 samples) currently lies at a shallower level (2000–8000 feet (600–2500 m) true vertical depth versus 8000–13,000 feet (3500–4000 m) in the northern suite of 27 samples), owing to a steeper uplift history in the south (Fall et al., 2015).

Consistent with previous SEM-CL surveys from the Piceance basin (Hooker et al., 2009), macroscopic fractures (Fig. 8a) are present amid parallel microfractures (Fig. 8d). Both size ranges contain quartz cement bearing assemblages of fluid inclusions, aligned generally parallel to fracture walls, and marked by parallel bands of crack-seal texture, apparent in SEM-CL (Fig. 8b). Dimly luminescent calcite cement overlaps quartz and generally does not show crack-seal banding (Fig. 8c). Larger microfractures (i.e., microscopic fractures wider than about 10 μm) and macrofractures are less likely to be entirely sealed by quartz, instead preserving considerable pore space or postkinematic calcite cement (Fig. 8).

Microfracture frequency was quantified by drawing scanlines on SEM-CL photomosaics constructed to form uninterrupted maps across core samples, perpendicular to fracture strike. Fig. 8d is a detail of one such image mosaic. Fracture intensity was then quantified by generating a cumulative frequency-aperture size plot (as in Fig. 2b) and best-fitting the *y*-intercept of a power-law equation having a slope (exponent) of −0.8, which is preferred when data are sparse (Hooker et al., 2014). This *y*-intercept is therefore equivalent to the predicted frequency of 1-mm-wide fractures, per mm of rock (Fig. 9).

The samples from the north and south fields of the Piceance basin derive from equivalent strata, but their current true vertical depths do not overlap (Fig. 9), owing to the aforementioned differential uplift (Fall et al., 2015). In both fields, we distinguished samples taken from below and above the top of continuous gas saturation, identified by Cumella and Scheevel (2008). The shallowest samples from either sample site are all among the lowest fracture frequencies observed: less than 0.002 fractures/mm. In contrast, deeper samples—those from below the top of continuous gas—show a wide range of fracture frequencies, from as low as that of shallow samples, to as much as 0.008 fractures/mm near the

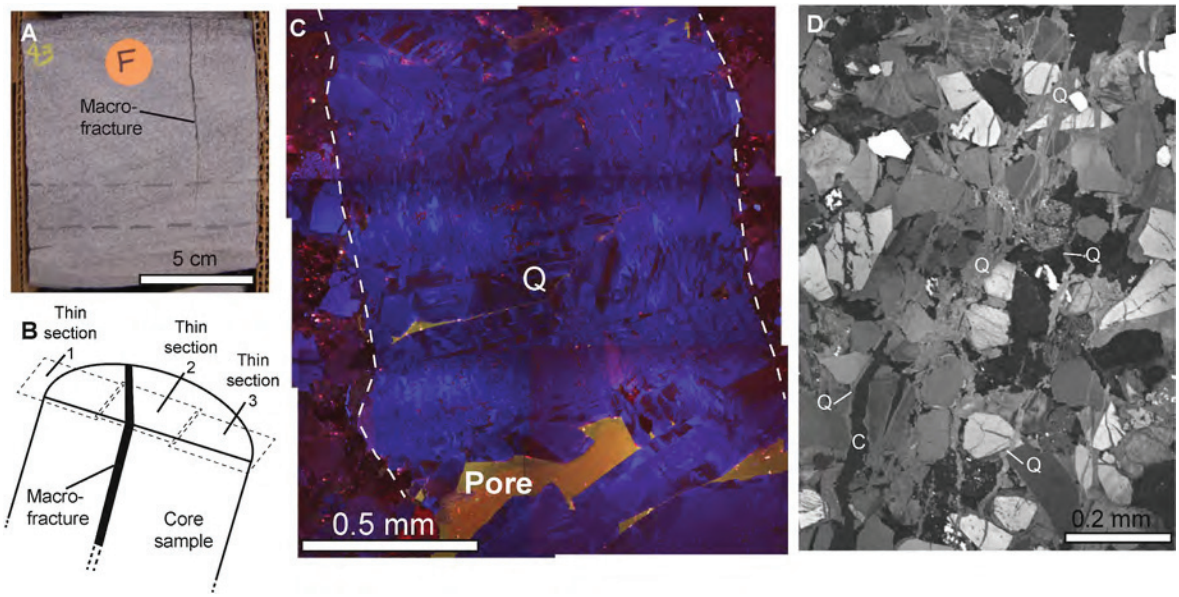

Fig. 8. Natural fractures, Piceance basin. (A) Vertical macrofracture in core, south Piceance basin. Macrofracture is partially filled by quartz crystals, not apparent at scale of photo. (B) Diagram of scanline geometry. Scanlines are made from SEM-CL images taken contiguously, parallel to layering, and across macroscopic fractures. (C) Color SEM-CL photomosaic of blue-luminescing quartz deposit (Q) bridging across vertical fracture, north Piceance basin. Fracture walls indicated by dashed lines. Pore space luminesces a yellowish hue. Crack-seal texture is present as fracture wall-parallel bands of blue quartz cement. (D) Grayscale SEM-CL image of a diffuse cluster of microfractures, north Piceance basin. Quartz fracture cement (Q) luminesces a medium gray. Relatively wide fracture at lower-left is lined with quartz and filled by non-luminescent, postkinematic calcite cement (C). Thinner microfractures are entirely filled by synkinematic quartz cement. (For interpretation of the references to color in this figure legend, the reader is referred to the Web version of this article.)

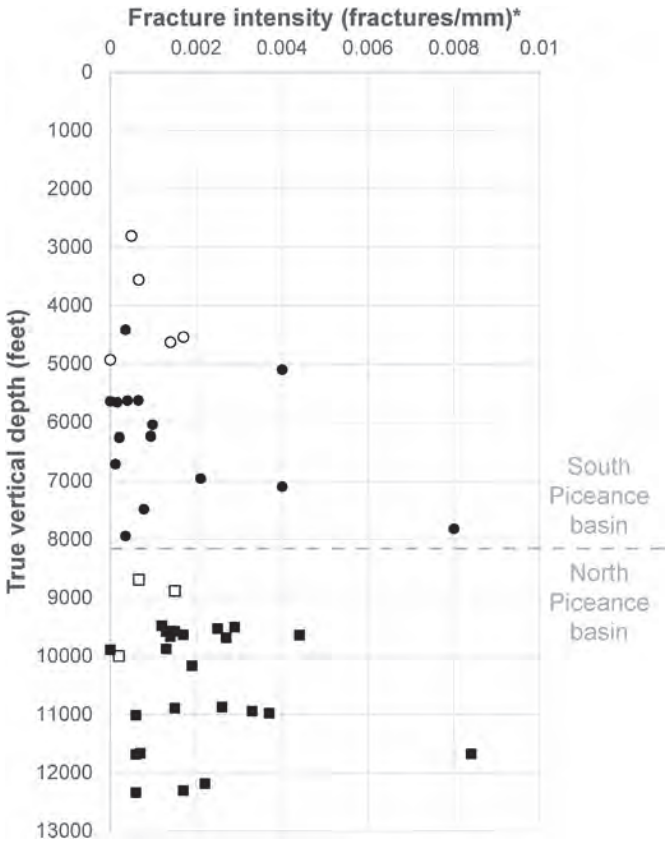

Fig. 9. Fracture intensity versus depth, Piceance basin. Intensity is calculated according to the method of Hooker et al. (2014)—see text. Circles, south Piceance basin (Fig. 7); squares, north Piceance basin; open symbols, samples above top of continuous gas saturation (Cumella and Scheevel, 2008); filled symbols, samples from within the gas-saturated zone.

greatest depths sampled (Fig. 9).

Interpretation. Crack-seal texture in quartz (Fig. 8c) indicates quartz precipitation during fracture opening that was rapid enough to span the gap from one fracture wall to the opposite wall, often at spatially isolated quartz deposits or bridges surrounded by pore space or post-kinematic calcite. Where crack-seal texture forms, continued opening of fractures apparently necessitates re-breaking of cements, based on crack opening increments within fracture-spanning cement deposits in Fig. 8c. In some cases, re-breaking is well localized within a single fracture, with little or no host-rock preserved amid successive fracture opening increments (Fig. 8c). In other cases, microfractures are present as clusters of distinct fractures, preserving host-rock in between (Fig. 8d). It was proposed that the degree of cementation itself plays some role in localization (Hooker et al., 2014), based on fracture traces that are locally diffuse, where spanning potential was high and crack-seal increments abundant, and locally discrete, where spanning potential was low and crack-seal texture rare. The interpretation was that high spanning potential promoted delocalization of progressive opening increments, and so affected both the size and spatial arrangement of fracture arrays (Hooker et al., 2014).

However, it is likely that such cements are only part of the story, and that inelastic processes such as chemically assisted cracking also play a role. For example, bridging cement deposits alone should not change the stress distribution around fractures, although they can modify the evolving stress field around fractures opening within a progressively extending host rock (Hooker and Katz, 2015). In contrast, subcritical cracking has been shown to enable a close spacing among fracture populations, as multiple nearby fractures can propagate simultaneously, before resulting stress shadows inhibit nearby fracture growth (Olson, 1993). These considerations motivate a new modeling approach to combined subcritical fracturing and cementation.

2.4. Summary of geologic examples

The evidence from the data collected points to a range of depth-related influences on the resulting fracture pattern. In the Scottish Highlands example, closely spaced, synkinematically cemented fractures have microscopic apertures and a tendency to open in crack-seal fashion, in which fractures reactivate without changing orientation, or causing slip on previous fractures. In contrast, macroscopically visible, partially open fractures grow to form complex networks in which fractures abut and reactivate one another, eventually coalescing to form faults.

In the Appalachian basin example, likely deep-seated, Group 3 and 2 cemented fractures are parallel and perpendicular to bedding. Lightly cemented, Group 1 fractures formed oblique to bedding in a thrust-faulting stress regime, likely at a late stage with respect to regional folding. Barren, Group 0 fractures formed parallel and perpendicular to bedding, despite bedding's oblique orientation with respect to the horizontal. Such a pattern could arise from shallow overburden and decoupling of bedding planes, which, in the absence of fast cementation or creep processes, created surfaces free of shear tractions that reoriented the stress field parallel to those surfaces.

In the Piceance basin, natural fractures are present in parallel arrays of widely spaced macrofractures and closely spaced microfractures. All fracture sizes include fracture-spanning cements, but the microfractures are more thoroughly filled by cements, pointing to a control on fracture size and spacing by those cements, and the degree to which fractures are sealed as they grow.

In all three cases, the depth of burial during fracture formation appears to have influenced fracture pattern development. Greater burial depth is expected to increase vertical compression and confining stress, one result of which is to inhibit slip along bedding planes and pre-existing fractures. Other possibilities exist as well, but we suggest that an underappreciated control on fracture patterns stems from temperature-dependent processes of cement precipitation and crack-tip corrosion reactions. Because all of these processes are expected to vary systematically with burial depth, their resulting effects on fracture pattern growth are difficult to understand in isolation, without modeling.

3. Spring lattice model

To explore the ramifications of this interpretation, we employ a numerical model that simulates both of the temperature-dependent, and therefore depth-dependent, chemical processes that are hypothetically at work during fracture pattern evolution: cementation of fractures and corrosive rock failure. Here we examine these effects in a hypothetical, structurally simple setting with steady lateral extension as a boundary condition. To fully recreate the complex deformations that occur in nature, particularly in compressional belts like our Caledonian and Alleghanian examples above, would require more robust modeling that is beyond our present scope. The model we employ extends the numerical model of Hooker and Katz (2015), which simulated a hexagonal spring lattice (Fig. 10) whose interconnected springs display linear-elastic behavior. Specifically:

$$F_{ij} = k_{ij}\,\delta\Delta_{ij} \tag{2}$$

where F is the force exerted by the spring, k is the spring constant, $\delta\Delta$ is the change in spring length from its equilibrium length, and subscripts i and j refer to spring positions within the lattice (Fig. 10). The model simulates extension fracturing by subjecting the lattice to a constant along-layer extension rate, V, as a boundary condition. The springs within the fracturing layer have a finite breaking strength,

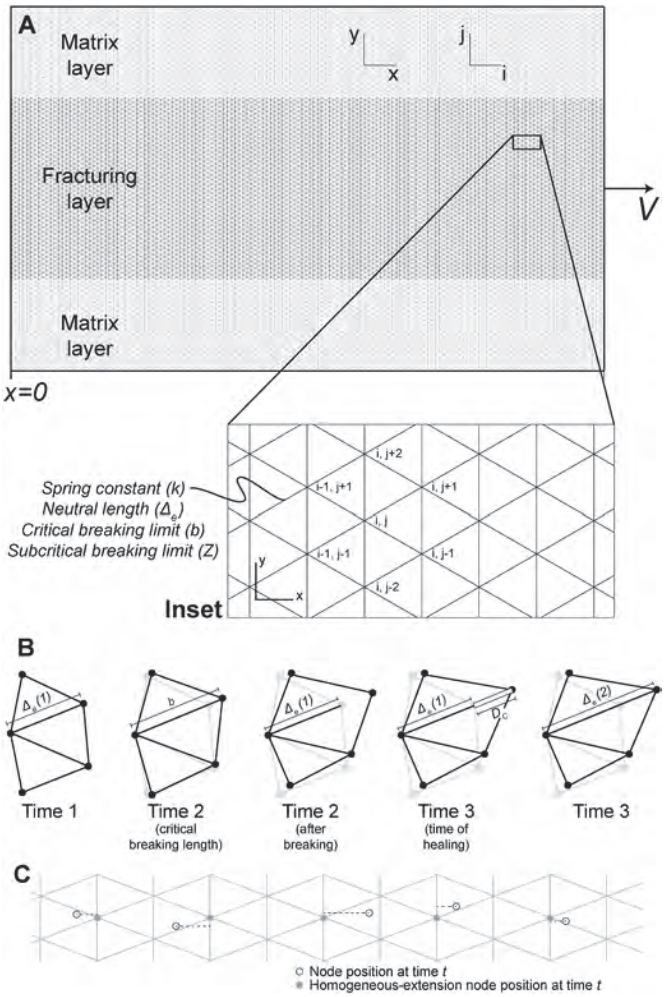

Fig. 10. Spring lattice model. (A) Layer setup. Three layers are composed of springs. The layers are stretched in the +x direction at constant rate. Springs in the matrix layers are indestructible; springs in the fracturing layer break once their critical breaking length (b) or subcritical failure integral (Z) is exceeded. Inset: Detail of spring lattice at initiation. (B) Breaking and cementation procedure. At Time 1, five nodes are connected by springs at their default spring constants (k) and neutral lengths, Δ_e. Reference position of springs and nodes shown in pale gray at later times. At Time 2, one of the springs is stretched to its elastic limit (length = b). The spring fails and the nodes move in response to force balance. The broken spring snaps back to its neutral length from Time 1. The spring grows via cementation at a constant rate, f. By Time 3, the spring has grown far enough to reach the separated node. At this time, the spring is re-attached with its original spring constant k and a new neutral length is assigned. (C) Quantification of strain heterogeneity, Q. Dashed lines represent the difference between the actual x coordinate and the homogeneous-strain x coordinate of each node along the middle row ($j = Nj/2$, rounded up). Q is the sum of each such difference, divided by ($Ni \times Nj$).

corresponding to a maximum length b the springs can attain before breaking:

$$\Delta_{ij}^{0} + \delta\Delta_{ij} = b_{ij} \tag{3}$$

where Δ^0 is the initial spring length, and also the starting equilibrium length. Springs within the matrix layers are indestructible.

Fractures form when sets of adjacent springs fail; heterogeneity in strength is introduced either through randomly distributed pre-broken springs, variation in critical breaking length b, or variation in spring constant k. Hooker and Katz (2015) introduced cementation by re-growing broken springs at a constant rate f, restoring the strength of the spring once its new length Δ' reconnects across the gap between the nodes it previously connected, pre-failure:

$$\Delta_{ij}^{'} = \Delta_{ij} + ft_{ij}^{*} \tag{4}$$

where t^* is the time since failure. At that moment of re-connection, a new neutral length is set to the current length of spring. The model is non-dimensionalized by normalizing all lengths to the initial spring length Δ^0; model time is scaled to $t = \Delta^0/V$; spring constants are rescaled by a reference value k^0; forces are then rescaled by $k^0\Delta^0$. Full model details, including implementation of the boundary conditions, are given in Hooker and Katz (2015).

The numerical experiments of Hooker and Katz (2015) suggested that, holding all else constant, both fracture aperture and spacing can be expected to decrease with increasing cementation rate.

This model is a simplification of nature in many respects, most especially in its assumption that deformation is purely elastic in settings in which fractures grow and fill with mineral cements. Here we extend this model by including a term that is intended to simulate time-dependent dissolution reactions that are thought to be particularly active at the highly tensile regions near fracture tips, and especially where pore fluids are acidic or high-ionic-strength brines at elevated temperature (e.g., Rinehart et al., 2016). Such dissolution reactions have been invoked to promote subcritical crack propagation (Atkinson, 1984). Subcritical crack growth, by corrosive reactions concentrated at crack tips, is likely a key process in natural fracture formation, based on the very slow growth of natural fractures inferred from fluid inclusion studies (e.g., Becker et al., 2010), including those of crack-seal fractures in the Piceance basin strata studied here (Fall et al., 2015). Corrosion reactions would also provide a potential source of silica for the quartz cement observed in the sandstone fractures of this study (Figs. 2 and 8).

We enable subcritical spring failure in the model by adding a second, time-dependent spring-failure criterion. Specifically, we integrate the force that accumulates on each fracturing-layer spring with respect to time, and require that springs fail once this integral exceeds a predefined value, Z:

$$\int F_{ij} dt_{ij}^{*} > Z_{ij} \tag{5}$$

This integral increases in value so long as the spring is longer than its neutral length. This failure criterion is therefore an accumulated time-stress integral, rather than simply a critical value of stress alone. Both failure criteria lead to fracture propagation, because tensile stresses tend to accumulate at fracture tips. The Z criterion can simulate time-dependent reactions that assist fracture propagation. Springs that fail according to Eq (4) are said to have failed subcritically, by analogy to rock fractures that propagate at lower stresses than those required to rupture bonds at fracture tips.

Of critical interest is how the size and spacing of fractures vary. We quantify resulting failure patterns based on the x-coordinates of nodes along the middle row of our fracturing layer.

$$Q = \frac{\sum |x - x_{hom}|}{Ni \times Nj} \tag{6}$$

where x-x_{hom} is the difference between a node's x coordinate and the x coordinate it would occupy if deformation were homogeneous (Fig. 10c). We design our statistic to reflect the geometry of the fractures within the bed, rather than the resolution of the nodes. Dividing by Ni averages the excess displacement among the nodes, and so controls for the horizontal resolution of the model space. Dividing by Nj normalizes the excess displacement to the layer thickness. This step is important because we anticipate that fracture width scales with length and therefore layer thickness.

We track a quantity analogous to porosity in the model as the sum of all broken spring lengths divided by the sum of all spring lengths, within the fracturing layer. These broken springs mechanically represent the uncemented parts of fractures and, at the initiation of model runs, the

flaws dispersed throughout the host rock.

We ran a suite of 20 simulations (Table 3) aimed at investigating fracture opening at varying values of depth and thus temperature. We hypothesize that increasing temperature increases kinetic reaction rates, thereby increasing cement precipitation rates and subcritical failure rates. We implement the former by increasing f, which seals fractures more quickly, and we implement the latter by decreasing Z, which promotes subcritical failure. Parameters used in the simulations for this study are listed in Table 3.

4. Results

Fig. 11 shows the state of the spring lattice at a final layer-parallel stretch (final length divided by initial length) of 1.6 for various values of subcritical failure criterion Z and cementation rate f. This large stretch was used so that the locations of fractures would be clear while using a relatively low-resolution, computationally efficient lattice. The model contains no specific definition of a fracture, although arrays of broken or re-healed springs can be recognized as extending vertically, or approximately so, across layering (Fig. 11).

Cementation rate f increases toward the right in Fig. 11; Z decreases downward. Therefore the two hypothetical effects of increasing depth—faster cementation and faster breakage by subcritical failure—increase downward and to the right in the figure. At the top left, the spring failures manifest primarily as isolated fractures that are wide and widely spaced, and that span the fracturing layer from top to bottom. Cementation and subcritical breakages are absent. At the bottom right, deformation is close to homogeneous. Most springs are currently cemented; a subset is currently broken via subcritical failure, and these latter are homogeneously distributed throughout the lattice. Discrete fractures are not present.

At intermediate positions, fractures are present, but tend to be smaller, compared to the shallow end-member. Fractures also have a wider range of widths, lengths, and spacings—particularly for $f = 10$, $Z = 6$. Where cementation is slow and subcritical cracking dominates (e.g., $f = 0.1$, $Z = 1$), fractures are commonly shorter than the fracturing-layer height, showing a tendency to branch.

Because spring strength is re-established upon cementation, cemented springs can re-fracture (Fig. 12). This behavior is analogous to crack-seal deformation, visible as myriad fracture opening increments having microscopic widths, but that form side-by-side, thereby comprising larger composite fractures (Fig. 8). We track the number of times each individual spring breaks throughout the simulation, sampling for new breaks with each recorded model output, which we make at regular intervals during extension. Re-breaking is common, particularly along bed-boundaries at moderate f (Fig. 12; $f = 1$, $Z = 6$, 10); throughout large veins at high f (Fig. 12; $f = 10$, $Z = 6$, 10); and throughout the entire fracturing layer at low Z (Fig. 12; $f > 0.1$, $Z = 0.1$).

High-resolution images from Figs. 11 and 12 illustrate some salient outcomes of the simulation (Fig. 13). In our shallowest simulation ($f = 0.1$, $Z = 10$), spring failures are abundant at the boundary between the fracturing and matrix layers, and healing is virtually absent (Fig. 13a and b). Fractures centered at these layer-boundary breakages are nearly box shaped, in that there is very little tapering of the fracture walls from the center of the fracture toward the tips. Holding Z constant but increasing cementation rate f to 10, fractures are more tapered, and failures along the layer boundaries are readily apparent (Fig. 13c), but they heal repeatedly throughout the simulation (Fig. 13d). Indeed, more healing-rebreaking episodes are apparent near fracture tips and layer boundaries, compared to fracture centers.

The effect of decreasing Z, thus accelerating subcritical failure, on fracture propagation, can be appreciated by comparing Fig. 13a and e. In the latter figure, in which $Z = 0.1$ and $f = 0.1$, healed springs are common only in the host rock, where displacement between neighboring nodes, beyond their initial separation, is negligible. These springs broke because the subcritical failure criterion will be reached even with tiny amounts of elastic lattice-extension, given sufficient time. Upon breakage, the extension (and hence tensile stress) between neighboring nodes was so small that breaking of the spring resulted in only a small change in node position, and the gap between the nodes was quickly healed, even under a slow cementation rate. Amid this relaxed stress state in the host rock, fractures tended to grow gradually, via a combination of subcritical and critical spring breakages. As a result, fractures are numerous and narrow, with a tendency to branch and cluster (Fig. 13e), compared to the high-Z default (shallow) scenario (Fig. 13a).

As f approaches infinity and Z approaches zero, the lattice extends homogeneously (Fig. 11, bottom-right). Here all nodes approach the subcritical failure criterion at low lattice extension, and the propagation of failures that produces fracturing in higher-Z simulations is minimized because abundant subcritical failures happen at such small lattice-extension values that little tensile stress is imparted to neighboring springs upon breakage. As we discuss below, this model space is analogous to cleavage formation at great depth. But, at intermediate f and Z values (e.g., $f = 1$; $Z = 3$), simulating depths where both cementation and subcritical fracturing exert a modest effect with neither overpowering the other, patterns emerge wherein fractures have a wide range of sizes and spacings (Fig. 13g). Here large fractures span the entire fracturing layer and preserve porosity, especially near the center, where fractures are widest. These large fractures are surrounded by small, mostly sealed, microfractures, which manifest as linear arrays of broken and re-healed springs, which generally do not extend across the entire fracturing layer (Fig. 13g).

Fig. 14 graphs the strain heterogeneity index Q and porosity as a function of stretch (final layer length divided by initial layer length) for each simulation. Each simulation begins with a porosity of approximately 0.1, a consequence of setting B^* to 0.1; i.e., beginning with 10% of springs broken. This step helps introduce heterogeneity at an early stage and tends to stabilize convergence of numerical solutions. With progressive cementation, this initial porosity declines to near 0; with increasing cementation rate, the initial porosity does not appear in Fig. 14, having already been filled by cement by the model time at which results are extracted for the plot.

At low cementation rate f and high subcritical failure criterion Z (i.e., shallow-level simulations), porosity and strain heterogeneity both tend to increase over time, after the initial porosity decrease (Fig. 14; $f = 0.1$, $Z = 10$). The effect of decreasing Z is to moderate porosity, such that it initially spikes and then declines to roughly a steady-state value (Fig. 14, $f = 0.1$; $Z = 0.1$, 1). At very low Z, strain heterogeneity likewise reaches a plateau early in the simulation (Fig. 14; $f > 0.1$, $Z = 0.1$). The effect of high f, relative to the shallow case, is mostly to decrease porosity. Pore space opens rapidly as fractures repeatedly open, then the fractures quickly seal, producing a spiky signal with troughs near 0 (Fig. 14; $f = 10$, $Z > 3$). In these simulations, strain heterogeneity produces a stair-step pattern, with discrete jumps in heterogeneity coinciding with positive spikes in porosity, which mark the opening of fractures. At deep simulations with high f and low Z, porosity tends to oscillate with amplitude that decays toward a steady state, amid generally

Table 3
Model parameters.

Parameter	Explanation	Number/Range used
Ni	Number of nodes in x direction	60
Nj	Number of nodes in y direction	90
Nj_b	Number of nodes in matrix layers	15
Wk	Spring constant distribution parameter	5
kpa	k perturbation amplitude	0.5
B^*	Fraction of fracturing-layer springs initially broken	0.1
b_m	Breaking length minimum	0.2
Z	Subcritical breaking integral minimum	–[0.1,1,3,6,10]
f	Cement accumulation rate	–[0.1,0.5,1,10]

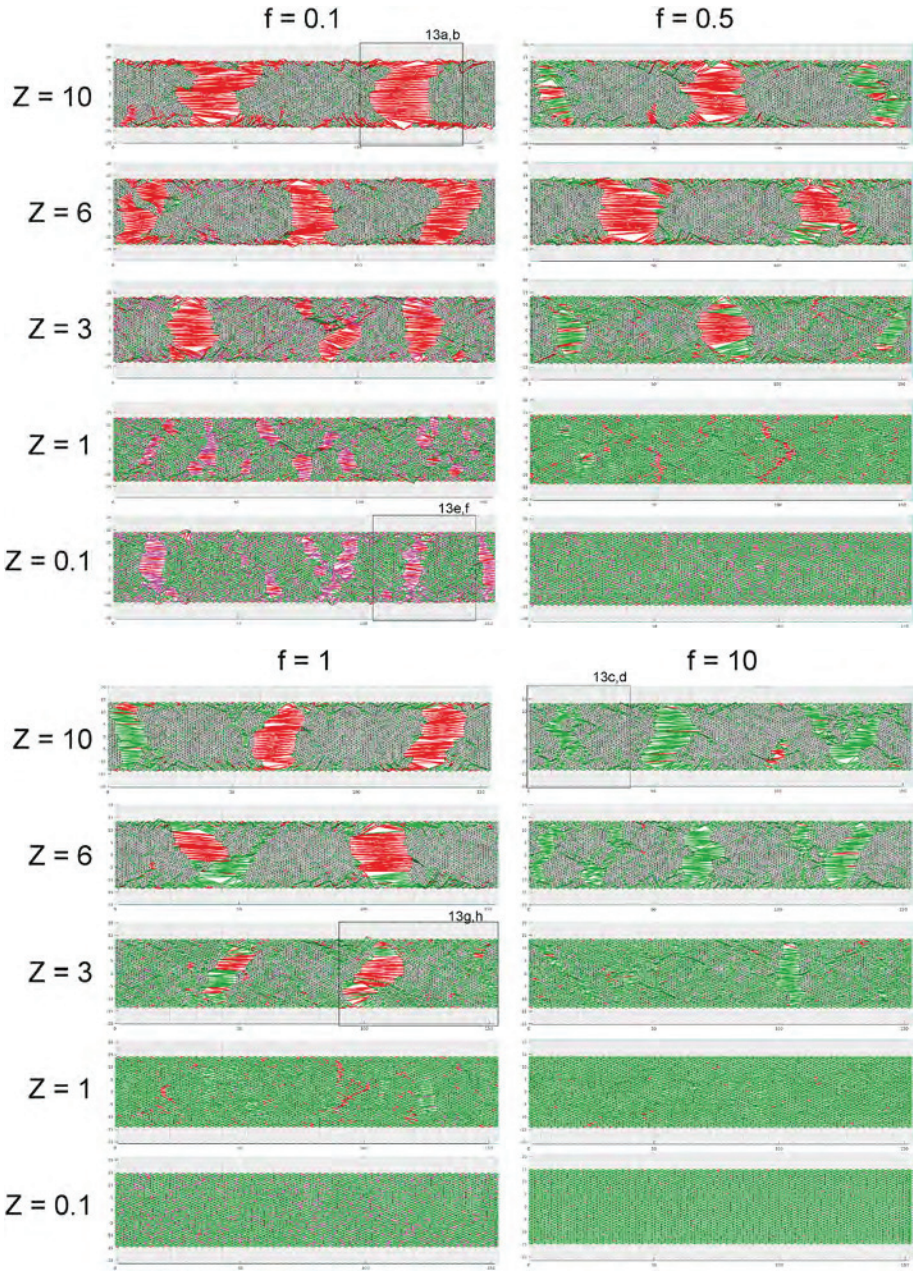

Fig. 11. Springs simulation results. Unbroken springs are black; healed springs are green; broken springs are red if broken by overextension, magenta if broken subcritically. Unbreakable matrix-layer springs, in gray, lie above and below the fracturing layer. Locations of detailed lattice areas in Fig. 13 shown. (For interpretation of the references to color in this figure legend, the reader is referred to the Web version of this article.)

synchronous fluctuations in strain heterogeneity (Fig. 14; $f > 0.1$, $Z = 0.1$).

5. Discussion

Our model produces different types of patterns (Figs. 11 and 12) that would correspond to different temperature-pressure-composition conditions. The results therefore delineate what we call *fracture facies*, based on the fracture patterns' relationships to the environmental formation conditions. "Fracture facies" is also used where fracture patterns are particular to the hosting sedimentary facies (e.g., Bruna et al., 2015; Li and Robinson, 2018), and so this term could also be applied to metamorphic facies. The physical constituents of any rock will control its mechanical properties and therefore influence its fracturing behavior, at a given temperature and pressure. Moreover, rock composition also affects mineral spanning potential through the inherent growth anisotropies of various minerals as well as the tendency of some minerals to preferentially accumulate on certain substrates (Lander and Laubach, 2015). Our modeling work addresses the potential for temperature and pressure to affect fracture patterns through their effects on chemical reactivity.

Moving from shallow (low cementation rate f, high subcritical failure criterion Z) to deep (high f, low Z) end-members of our simulations produces a spectrum of fracture patterns (Fig. 15). At the shallow extreme, fractures are discrete arrays of broken springs having wide spacings, simple geometries, and large amounts of porosity (Fig. 14). We refer to this end-member pattern development as "exclusionary macrofracturing." Here fractures tend to propagate the entire vertical distance across the fracturing layer, and the resulting relief of tension creates an exclusionary zone or stress shadow to either side, in which the opening

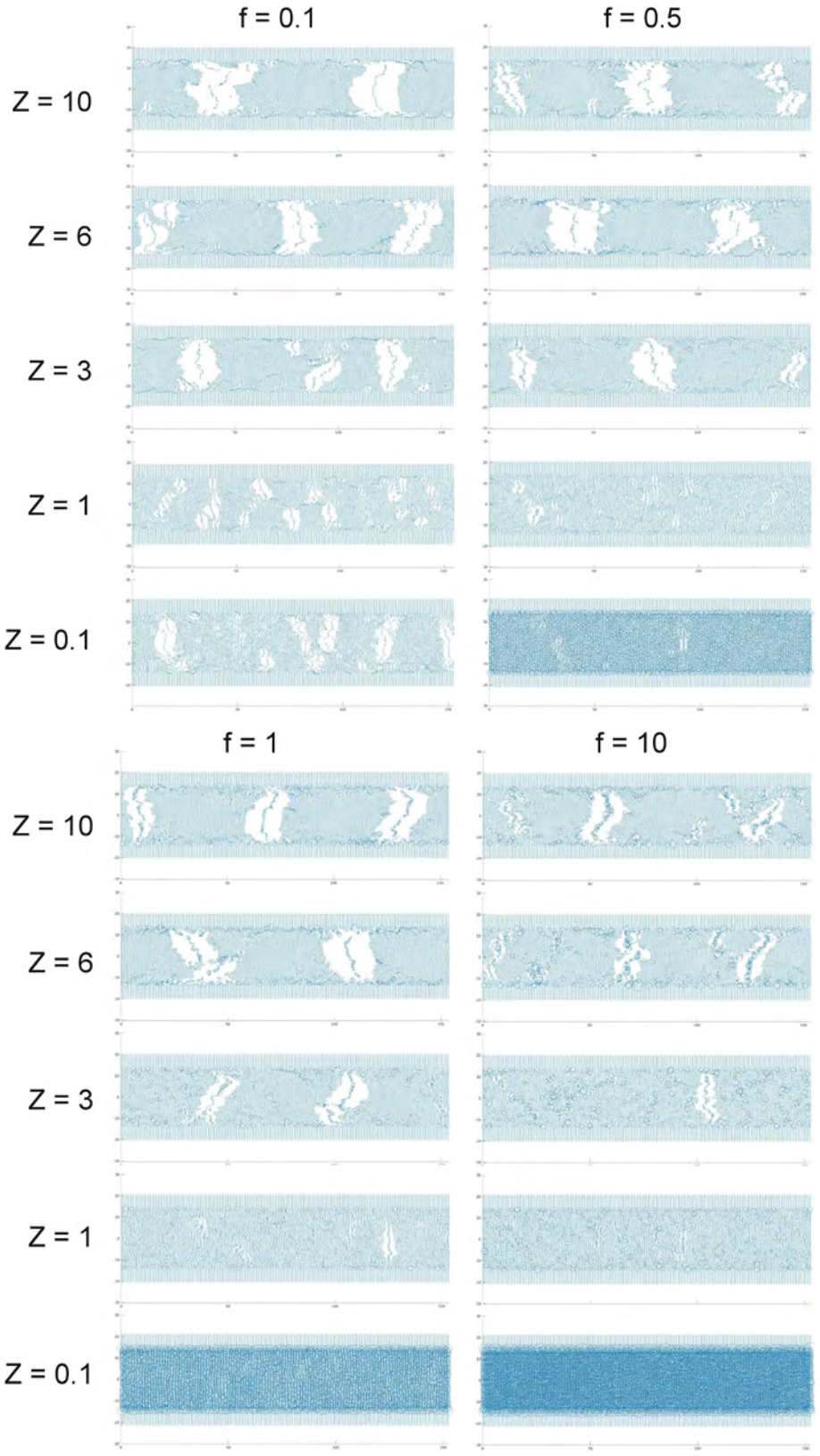

Fig. 12. Spring lattice simulation results. Circle diameter proportional to the number of times a spring has broken.

of new fractures is suppressed. In such cases of low *f* and high *Z*, fracture size, spacing, and porosity distribution-evolution are unaffected by chemical processes.

At the deep extreme (Fig. 15, bottom-right), the model does not produce isolated fractures, but instead the neighboring node-separation is close to uniform. Cementation is rapid and springs readily fail sub-critically, such that springs break and re-seal many times throughout the simulation, without the buildup of large stress concentrations. Strain

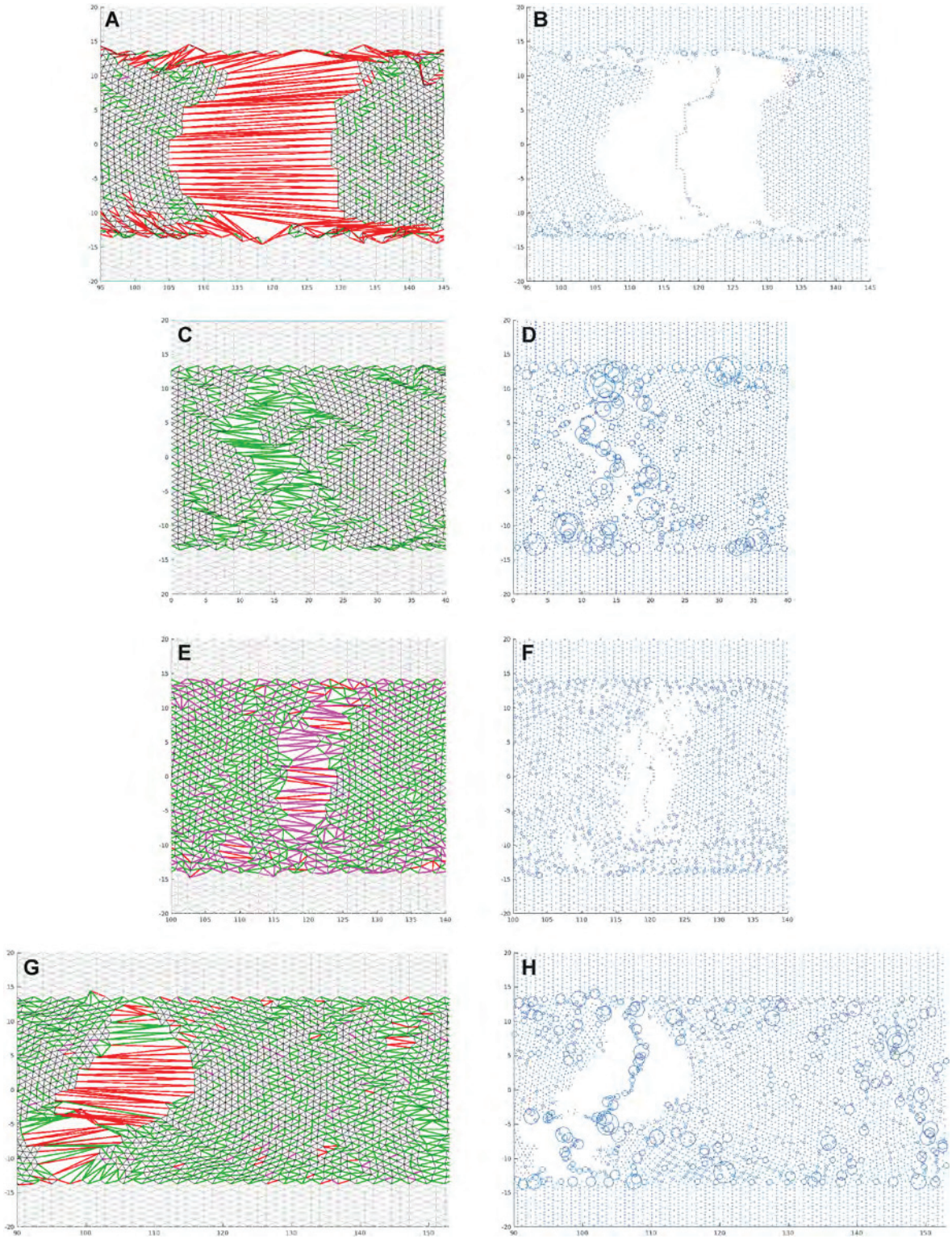

Fig. 13. Details of spring lattices from model output. (A, C, E, G): springs, colors as in Fig. 11). (B, D, F, H): circle size proportional to number of times broken, as in Fig. 12. See Fig. 11 for locations and text for discussion. (For interpretation of the references to color in this figure legend, the reader is referred to the Web version of this article.)

heterogeneity and porosity are low and reach their maxima early in the simulation (Fig. 14 $Z = 0.1$, $f = 10$). This behavior mimics the development of myriad very closely spaced, sealed fractures, which have been noted in sandstones (Laubach, 1989; Onasch, 1990; Hooker et al., 2014; their Fig. 11b) and limestones (Davis, 2014; Hoyt and Hooker, 2021; their Figure 16). The texture sometimes forms at the slow-opening tips of tectonic "stretching veins" (Bons et al., 2012; their Figure 17b). The rock deformation and evolving stress distribution in such cases is akin to that which develops in compressive environments as a disjunctive cleavage (Engelder, 1979). There, dissolution of soluble material from closely spaced, microscopic surfaces achieves a volume loss. Based on the similar distribution of structures, only here resulting from extension and

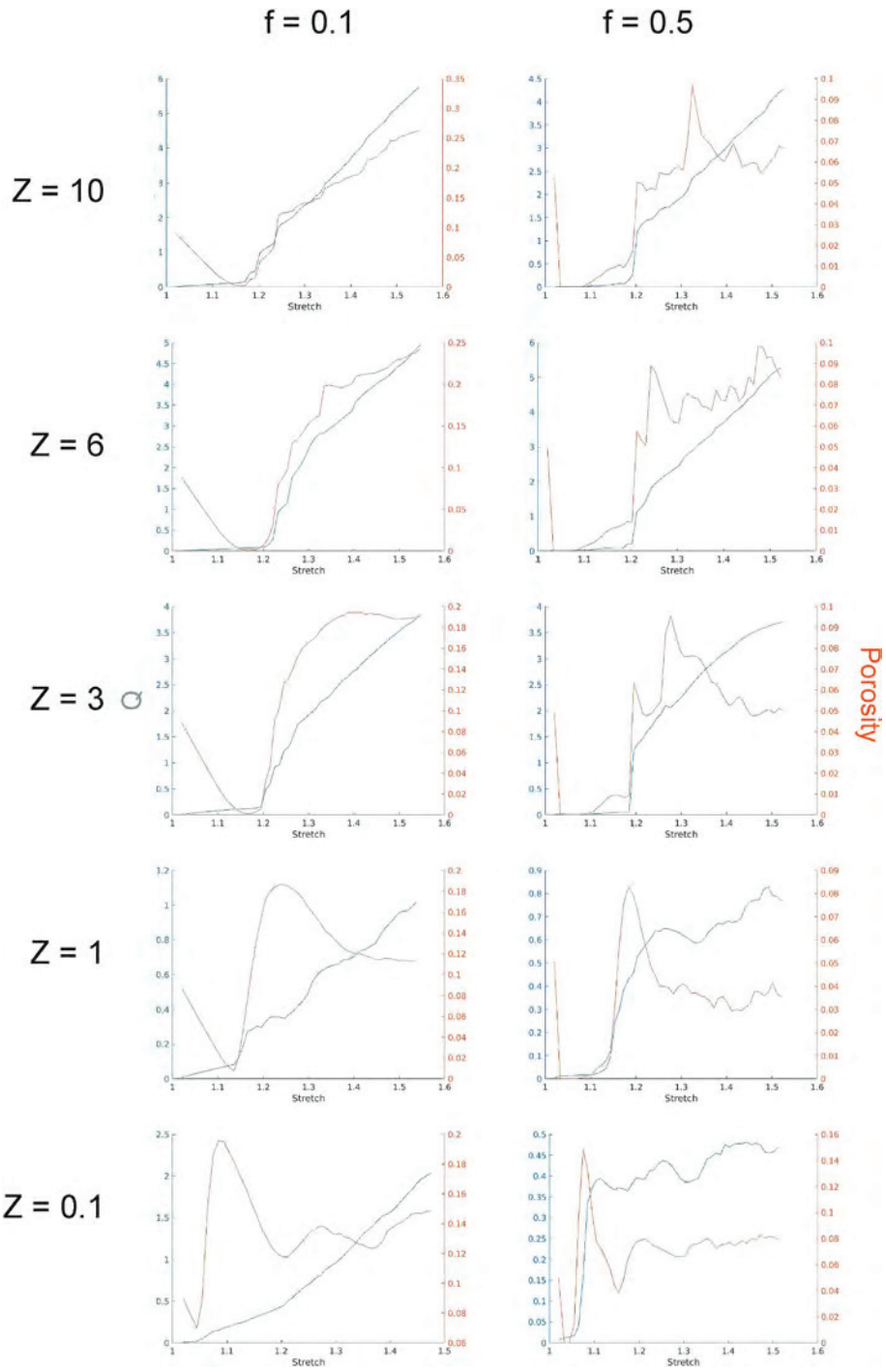

Fig. 14. Spring lattice simulation results. Porosity and strain heterogeneity (Q) plotted versus stretch, which is equivalent to model time.

rapid cementation of ephemeral fracture pore space, we term this behavior "penetrative microfracturing."

For exclusionary macrofracturing, note that we anticipate layer delamination to be an important process in halting fracture propagation (Fig. 15), consistent with model results (Figs. 11, Figure 12, Fig. 13). We also note open fractures in the Dundonnell outcrop are more likely to halt, or deflect, the propagation of later intersecting fractures, compared to the small halting power of cemented fractures (Fig. 3). Likewise, we hypothesize that delamination may be relatively important for the orientation of uncemented fractures in the Marcellus core samples we documented (Fig. 6). Delamination tends to be suppressed via cementation with higher f (Figs. 11, Figure 12, Fig. 13). Our choice to make matrix layers indestructible forces fracturing to continue, even to great width/height ratios, in all simulations, but in reality, those matrix layers would eventually fail, and likely at lower extension values in cases where cementation precludes delamination and layer-parallel sliding.

At intermediate positions on the spectrum, rock failure and cementation are relatively balanced, in the sense that some growing fractures become sealed while others remain open. Resulting fracture sizes and spacings are more variable (Fig. 15 c-h). Large fractures form amid clusters of small fractures, and many fractures do not extend all the way across the fracturing layer (Fig. 11). Although our model resolution is

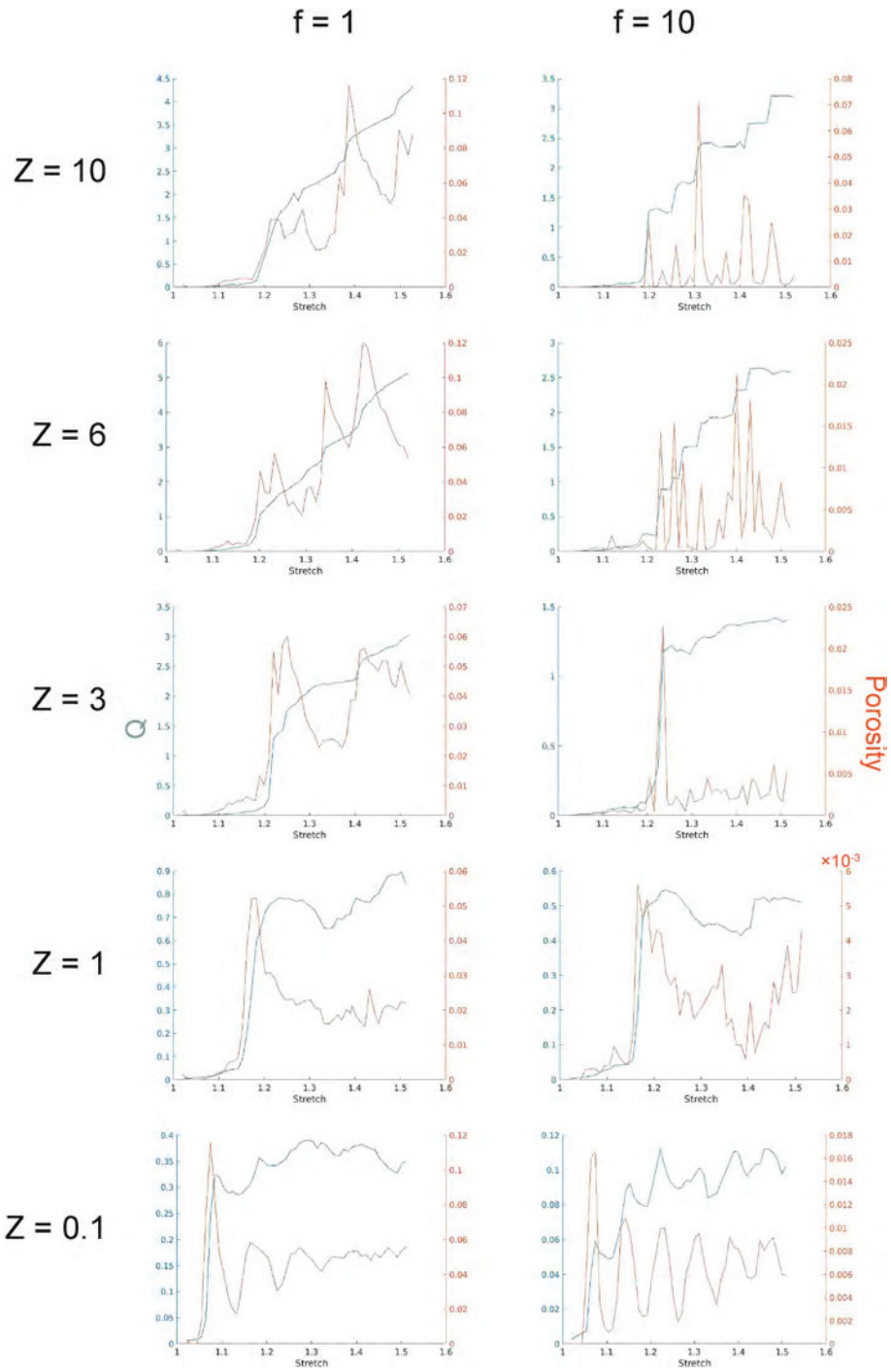

Fig. 14. (*continued*).

insufficient to illustrate fracturing opening over multiple orders of magnitude, the relatively wide range of widths produced is analogous to the power-law size distributions of kinematic apertures commonly observed among cemented fractures (Fig. 2b). Such fractures also commonly contain crack-seal cements, implying multiple episodes of re-cracking, as observed at high *f* (Fig. 12). We term this fracture facies "multi-scale" fracturing.

The extreme off-axis positions, namely, positions C and G in Fig. 15, reflect conditions for a combination of shallow and deep settings, but may nonetheless correspond to natural fracturing environments. In Fig. 15c, cementation is rapid yet subcritical failure is minimal. Such a situation could correspond to shallow geothermal reservoirs, in which hot, mineral-laden fluids invade an otherwise cool rock body. Here cement precipitation can strengthen the rock, including within previously open fractures (Laubach, 1988; Laubach et al., 2009; Major et al., 2018; Callahan et al., 2019a), at shallow levels in which host-rock deformation is close to elastic (Callahan et al., 2019b).

A useful metric for judging 'rapid cementation' and its contrasts with depth and rock type is spanning potential (Lander and Laubach, 2015). Although the example in that paper is specifically quartz, the principle is the same for all mineral systems. For a constant, temperature based mineral accumulation rate and fractures opening at the same rate, rock composition can lead to differences in mineral spanning. For example, in sandstones, quartz has diminished spanning (lower overall

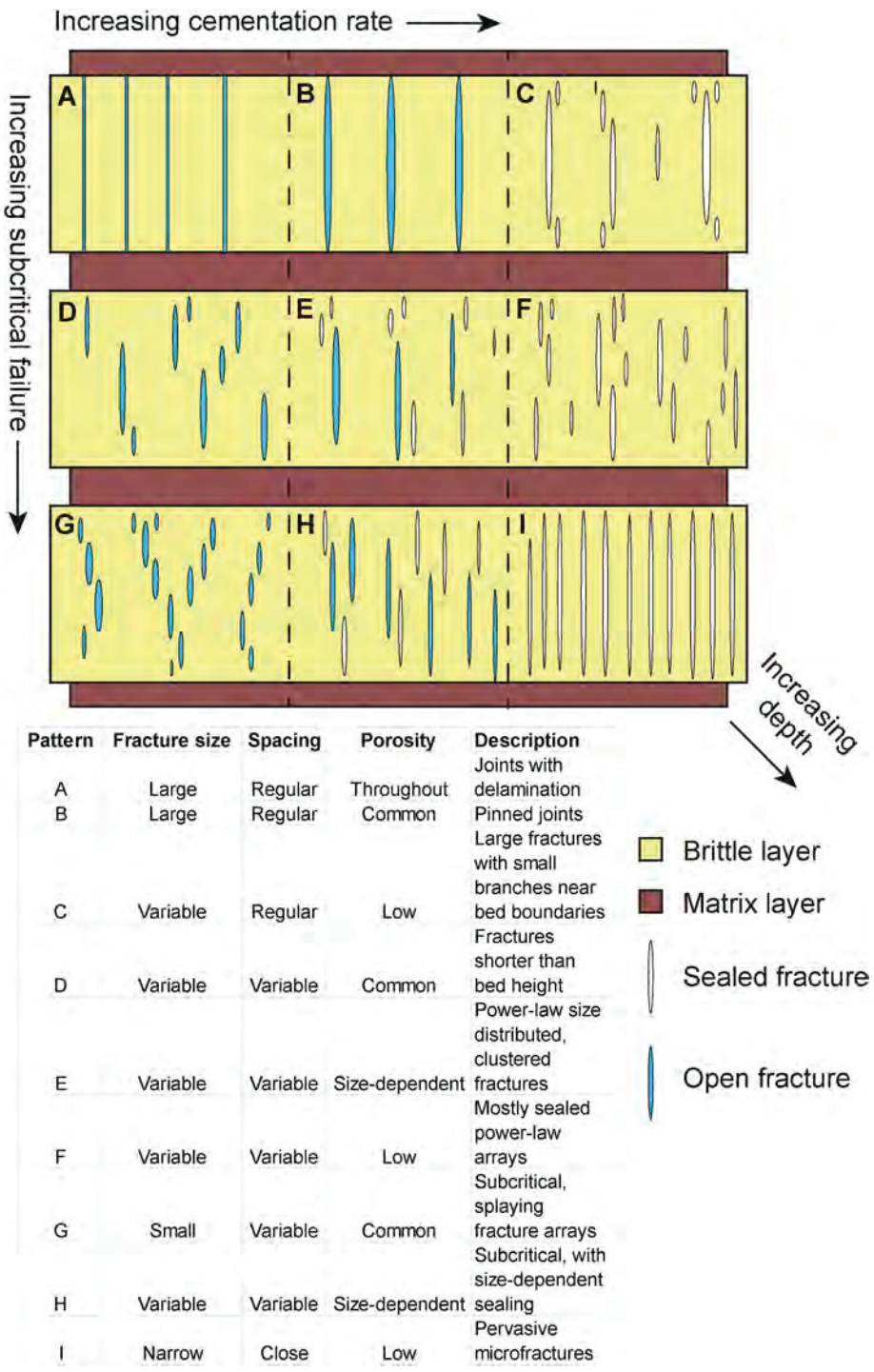

Pattern	Fracture size	Spacing	Porosity	Description
A	Large	Regular	Throughout	Joints with delamination
B	Large	Regular	Common	Pinned joints
C	Variable	Regular	Low	Large fractures with small branches near bed boundaries
D	Variable	Variable	Common	Fractures shorter than bed height
E	Variable	Variable	Size-dependent	Power-law size distributed, clustered fractures
F	Variable	Variable	Low	Mostly sealed power-law arrays
G	Small	Variable	Common	Subcritical, splaying fracture arrays
H	Variable	Variable	Size-dependent	Subcritical, with size-dependent sealing
I	Narrow	Close	Low	Pervasive microfractures

Fig. 15. Conceptual diagram of the effects of subcritical failure and cementation on extensional fracture patterns. Note correspondence in axes with Figs. 11, 12 and 14. With increasing depth and temperature, we move toward the lower-right on the diagram. Nine patterns or fracture *facies* (A through I) illustrate fractures forming in a brittle layer encased within unfractured matrix layers. White fractures are entirely cement-filled; blue fractures are at least partially open. Hypothetical shallowest-forming fracture pattern is (A), here the "exclusionary macrofracturing" facies, and both cementation and subcritical failure increase with depth. We therefore expect increasing burial depth to correspond to a shift toward the lower-right on the diagram, through the "multi-scale" facies (E) and beyond to the "penetrative microfracturing" facies (I). See text for description and interpretation of the remaining facies. (For interpretation of the references to color in this figure legend, the reader is referred to the Web version of this article.)

accumulation) in feldspathic sandstones compared to quartzose sandstones owing to slower accumulation of quartz on feldspar substrates. Laubach et al. (2014) describe adjacent sandstones cut and fractured by the same faults that have different spanning owing to contrasts in feldspar content, and associated differences in aperture size distributions. Likewise, in shales and other fine-grained rocks, spanning is suppressed by crystals nucleated on small substrates achieving slow euhedral growth rates sooner (Lander and Laubach, 2015). As with metamorphic facies, rock composition as well as thermal history can influence what constitutes a facies boundary. Thermal exposure often exerts the greatest control; therefore, where geothermal gradients are low, such as the Tarim basin of China (Laubach et al., 2023), we expect deep-seated occurrence of "shallow" fracture facies.

Fig. 15g represents a case of rock readily failing subcritically where cementation is slow. Such a situation might be present in the deep subsurface where cementation is suppressed, whether by the presence of hydrocarbons or other nonaqueous pore fluids, or where clay minerals coat potential templating surfaces such as quartz grains. High hydrocarbon saturation was invoked as a mechanism to preserve uncemented joints through the development of a penetrative cleavage in black shales and siltstones in the Appalachian basin (Engelder et al., 2001). Many of these fractures are present in variably layerbound, clustered arrangements (Tan et al., 2014), a pattern readily explained by subcritical crack growth (Olson, 1993). As well, Savalli and Engelder (2005) interpreted

smooth plumose texture and regular arrest lines as evidence that regional joints propagated subcritically.

Clay coatings were found to have preserved reservoir quality by inhibiting cement precipitation on sandstone grains in the Bonaparte basin of Australia (Saïag et al., 2016). The effect was demonstrated experimentally through growth of chlorite grain coatings by Charlaftis et al. (2021). Although fracturing generally exposes new surface area according to the composition of the grain that is cut, a pore fluid rich in suspended clays, or a fracture that preferentially propagates along clay minerals, could result in fracture opening amid limited cementation.

Another potential natural example of abundant subcritical crack growth paired with minimal cementation would be crevasses in glacier ice (Koehn and Sachau, 2014; Hudleston, 2015; Colgan et al., 2016). Here deformation is dominated by creep, such that ice bonds break and reform via inelastic processes. Although the micromechanics of creep are outside the scope of our modeling effort, at maximum susceptibility to subcritical failure (minimum Z) our lattice responds to extension in a similar manner, whereby elastic stresses are dissipated over time by myriad subcritical breakages and re-sealings (Fig. 11 bottom-left). Crevasses represent open fractures and so are "cemented" (filled by ice) only slowly, compared to their opening rates, if at all (Colgan et al., 2016). The topographic gradients involved in glacial creep exert a strong control on fracture propagation and morphology which we likewise do not address here. But with continued climatic warming, in which deformation processes may accelerate and ice growth within fractures is expected to diminish, the process of ice crevasse formation may be expected to move progressively toward the lower left of Fig. 15.

The limitations of our modeling approach are many, and worth reviewing, both for perspective about our interpretations and for potential future avenues of research. The model is 2-D, and so ignores pattern formation along fracture strike. The propagation of fractures along bedding likely produces considerably greater fracture interaction, which has been shown to materially affect pattern outcomes (Olson and Pollard, 1989; Cladouhos and Marrett, 1996).

Cementation of springs proceeds at a constant rate within each simulation. The assumption is that transport of mineralizing solutes is not rate-limiting, throughout the model. Instead, the precipitation step is assumed to be rate-limiting (Walderhaug, 1996; Lander et al., 2008). This case was called *reaction-limited* by Romano and Williams (2022). We base this assumption on textural evidence from synkinematically cemented sandstones, in which cement accumulation rates vary considerably by several aspects of the precipitation substrate. These aspects include grain size, mineralogy, and whether the growth surface is euhedrally or anhedrally terminated (Lander and Laubach, 2015). Including these various effects, as well as running transport-limited simulations, would allow us to simulate a wider range of possibilities, and possibly yield insights into important phenomena such as mineral-grain-scale effects on strain localization and porosity evolution (e.g., Vass et al., 2014; Liu et al., 2020; Monsees et al., 2021; Qin et al., 2022).

Our treatment of subcritical failure is intended to address a problematic simplification presented by previous similar models (e.g., Hooker and Katz, 2015). Nevertheless, our subcritical failure term, like our cementation rate term, remains a simplified representation of the natural process. Laboratory tests have shown that subcritical crack propagation is sensitive to both the host rock (Holder et al., 2001) and the fluid chemistry (Callahan et al., 2019b; Chen et al., 2020). Our model does not directly account for pore fluids, and so ignores any potential variability in space and time for susceptibility to corrosive reactions that lead to subcritical crack propagation (Atkinson, 1984).

Furthermore, by ignoring fluids, we ignore any dynamic effects that pore fluids might exert on the fracturing dynamics. Fluid pressures are thought to enable fracture opening at depth in general (Secor, 1965; Bons et al., 2022). In this light, our simulations can be thought of as an end-member scenario in which high host-rock permeability suppresses spatial variability in fluid pressure. If this were not the case, then cyclic interactions between fluid overpressure and fracture opening or slip (Lacazette and Engelder, 1992; Fischer et al., 1995; Olson, 2003; de Riese et al., 2020; Hooker and Fisher, 2021) could dominate fracture-opening sequences in ways that the present work does not illustrate.

6. Conclusion

Natural fracture arrays illustrate some of the many effects that depth of formation exerts on natural fracture patterns. Previous studies have documented physical, depth-related effects, including suppressing slip along bedding planes and pre-existing fractures via high confining stress. We presented a spring lattice model that incorporates two key thermochemical effects: synkinematic cementation, which provides adhesion across fractures, and subcritical failure. Although these effects are sensitive to the chemical environment dictated by host rock composition and fluid flow history, they are also promoted by high temperatures and high ionic-strength pore waters. These effects are therefore dependent upon thermal history, and thus in many cases burial history, suggesting that for opening-mode fractures at least, systematic size, spatial arrangement, and porosity patterns develop with depth (thermal exposure). We can categorize depth-dependent fracture patterns, for a given rock type, as *fracture facies*. Shallow (cool) environments with minimal effects of synkinematic cementation or chemically assisted cracking produce widely spaced, barren or minimally cemented joints ("exclusionary macrofracturing" facies). At intermediate depths, which, for a given rock type, geothermal gradient, and loading path, could range from 2 to 10 km, fractures that are moderately to extensively cemented during formation tend to have wide aperture size ranges, wide variability in spatial arrangement tending toward clustered patterns, and a considerable population of microfractures ("multiscale fracturing" facies). Model results and limited observations suggest that at high temperature patterns may develop having narrow aperture size ranges, decreased variability in spatial arrangement, and a preponderance of microfractures ("penetrative microfracturing" facies). Other regions of model space have the potential for representing shallow geothermal reservoir fracturing (fast cementation, resistant to subcritical failure) and cement-suppressed cases such as fracturing amid saturated hydrocarbons and ice crevasse formation (slow cementation, susceptible to subcritical failure).

Author statement

John Hooker: Conceptualization, Methodology, Software, Investigation, Writing, Visualization, Funding acquisition Rich Katz: Methodology, Software, Formal analysis, Writing Steve Laubach: Conceptualization, Investigation, Writing, Funding acquisition Joe Cartwright: Conceptualization, Resources Peter Eichhubl: Investigation, Writing Esti Ukar: Investigation, Writing Dana Bloomfield: Investigation, Writing Terry Engelder: Conceptualization, Resources.

Declaration of competing interest

The authors declare that they have no known competing financial interests or personal relationships that could have appeared to influence the work reported in this paper.

Data availability

Data will be made available on request.

Acknowledgments

JNH is supported by U.S. National Science Foundation Tectonics program grant EAR-2214325. Aspects of this study were supported by grant DE-SC0022968 from Chemical Sciences, Geosciences and

Biosciences Division, Office of Basic Energy Sciences, Office of Science, U.S. Department of Energy and by the Fracture Research and Application Consortium at The University of Texas at Austin.

References

Ankit, K., Urai, J.L., Nestler, B., 2015. Microstructural evolution in bitaxial crack-seal veins: a phase-field study. J. Geophys. Res. Solid Earth. https://doi.org/10.1002/2015JB011934.

Atkinson, B.K., 1984. Subcritical crack growth in geological materials. J. Geophys. Res. 89, 4077–4114.

Bai, T., Pollard, D.D., 2001. Getting more for less: the unusual efficiency of fluid flow in fractures. Geophys. Res. Lett. 28, 65–68.

Becker, S.P., Eichhubl, P., Laubach, S.E., Reed, R.M., Lander, R.H., Bodnar, R.J., 2010. A 48 m.y. history of fracture opening, temperature, and fluid pressure: Cretaceous Travis Peak Formation, East Texas basin. GSA Bulletin 122 (7–8), 1081–1093.

Berg, T.M., Edmunds, W.E., Geyer, A.R., Glover, A.D., Hoskins, D.M., MacLachlan, D.B., Root, S.I., Sevon, W.D., Socolow, A.A., 1980. Geologic Map of Pennsylvania (1: 250,000 Scale). Pennsylvania Geological Survey.

Bistacchi, A., Mittempergher, S., Martinelli, M., Storti, F., 2020. On a new robust workflow for the statistical and spatial analysis of fracture data collected with scanlines (or the importance of stationarity). Solid Earth 11, 2535–2547.

Bons, P.D., Elburg, M.A., Gomes-Rivas, E., 2012. A review of the formation of tectonic veins and their microstructures. J. Struct. Geol. 43, 33–62.

Bons, P.D., Cao, D., de Riese, T., González-Esvertit, E., Koehn, D., Naaman, I., Sachau, T., Tian, H., Gomez-Rivas, E., 2022. A review of natural hydrofractures in rocks. Geol. Mag. https://doi.org/10.1017/S0016756822001042.

Bruna, P.-O., Guglielmi, Y., Viseur, S., Lamarche, J., Bildstein, O., 2015. Coupling fracture facies with in-situ permeability measurements to generate stochastic simulations of tight carbonate aquifer properties: example from the Lower Cretaceous aquifer, Northern Provence, SE France. J. Hydrol. 529, 737–753.

Callahan, O.A., Eichhubl, P., Olson, J.E., Davatzes, N.C., 2019a. Fracture mechanical properties of damaged and hydrothermally altered rocks, Dixie Valley-Stillwater fault zone, Nevada, USA. J. Geophys. Res. Solid Earth 124, 4069–4090.

Callahan, O.A., Eichhubl, P., Olson, J.E., Davatzes, N.C., 2019b. Experimental investigation of chemically aided fracture growth in silicified fault rocks. Geothermics 83, 101724.

Charlaftis, D., Jones, S.J., Dobson, K.J., Crouch, J., Acikalin, S., 2021. Experimental study of chlorite authigenesis and influence on porosity maintenance in sandstones. J. Sediment. Res. 91 (2), 197–212.

Chemenda, A.I., Lamarche, J., Matoniti, C., Bazalgette, L., Richard, P., 2021. Origin of strong nonlinear dependence of fracture (joint) spacing on bed thickness in layered rocks: mechanical analysis and modeling. J. Geophys. Res. Solid Earth 126, e2020JB020656.

Chen, X., Eichhubl, P., Olson, J.E., Dewers, T.A., 2020. Salinity, pH, and temperature controls on fracture mechanical properties of three shales and their implications for fracture growth in chemically active fluid environments. Geomechanics for Energy and the Environment 21, 100140.

Cladouhos, T.T., Marrett, R., 1996. Are fault growth and linkage models consistent with power-law distributions of fault lengths? J. Struct. Geol. 18 (2/3), 281–293.

Clark, M.B., Brantley, S.L., Fisher, D.M., 1995. Power-law vein-thickness distributions and positive feedback in vein growth. Geology 23 (11), 975–978.

Colgan, W., Rajaram, H., Abdalati, W., McCutchan, C., Mottram, R., Moussavi, M.S., Grigsby, S., 2016. Glacier crevasses: observations, models, and mass balance implications. Rev. Geophys. 54, 119–161.

Corrêa, R.S.M., Marrett, R., Laubach, S.E., 2022. Analysis of spatial arrangement of fractures in two dimensions using point process statistics. J. Struct. Geol. 163, 104726.

Cumella, S.P., Scheevel, J., 2008. The influence of stratigraphy and rock mechanics on Mesaverde gas distribution, Piceance Basin, Colorado. In: Cumella, S.P., Shanley, K. W., Camp, W.K. (Eds.), Understanding, Exploring, and Developing Tight-Gas Sands: 2005 Vail Hedberg Conference: American Association of Petroleum Geologists Hedberg Series, vol. 3, pp. 137–155.

Davis, G.H., 2014. Quasi-flexural folding of pseudo-bedding. GSA Bulletin 126 (5–6), 680–701.

de Riese, T., Bons, P.D., Gomez-Rivas, E., Sachau, T., 2020. Interaction between crustal-scale Darcy and hydrofracture fluid transport: a numerical study. Geofluids 2020. https://doi.org/10.1155/2020/8891801.

de Joussineau, G., Petit, J.-P., 2021. Mechanical insights into the development of fracture corridors in layered rocks. J. Struct. Geol. 144, 104278.

Eichhubl, P., 2004. Growth of ductile opening-mode fractures in geomaterials. Geological Society, London, Special Publications 231 (1), 11–24.

Elmore, R.D., Burr, R., Engel, M., Parnell, J., 2010. Paleomagnetic dating of fracturing using breccia veins in Durness group carbonates, NW Scotland. J. Struct. Geol. 32, 1933–1942.

Engelder, T., 1979. Mechanisms for strain within the upper devonian clastic sequence of the Appalachian plateau, western New York. Am. J. Sci. 279, 527–542.

Engelder, T., Haith, B.F., Younes, A., 2001. Horizontal slip along Alleghanian joints of the Appalachian plateau: evidence that mild penetrative strain does little to change the pristine appearance of early joints. Tectonophysics 336, 31–41.

Engelder, T., Whitaker, A., 2006. Early jointing in coal and black shale: evidence for and Appalachian-wide stress field as a prelude to the Alleghanian orogeny. Geology 34, 581–584.

Engelder, T., Gross, M., 2018. Pancake joints in Utica gas shale: mechanisms for lifting overburden during exhumation. J. Struct. Geol. 117, 241–250.

Evans, M.A., 2010. Temporal and spatial changes in deformation conditions during the formation of the Central Appalachian fold-and-thrust belt: evidence from joints, vein mineral paragenesis, and fluid inclusions. In: Tollo, R.P., Bartholomew, M.J., Hibbard, J.P., Karabinos, P.M. (Eds.), From Rodinia to Pangea: the Lithotectonic Record of the Appalachian Region. Geological Society of America Memoir 206, pp. 477–552.

Evans, M.A., 2023. Syntectonic sediment loading and fold-thrust belt structural architecture: An example from the central Appalachians (USA). Geosphere. https://doi.org/10.1130/GES02573.1.

Evans, M.A., DeLisle, A., Leo, J., Lafonte, C.J., 2014. Deformation conditions for fracturing in the middle devonian sequence of the central appalachians during the late paleozoic alleghanian orogeny. AAPG (Am. Assoc. Pet. Geol.) Bull. 98 (11), 2263–2299.

Faill, R.T., 1998. A geologic history of the north-central Appalachians, Part 3. The Alleghanian orogeny. Am. J. Sci. 298, 131–179.

Fall, A., Eichhubl, P., Cumella, S.P., Bodnar, R.J., Laubach, S.E., Becker, S.P., 2012. Testing the basin-centered gas accumulation model using fluid inclusion observations: southern Piceance Basin, Colorado. AAPG (Am. Assoc. Pet. Geol.) Bull. 96 (12), 2297–2318.

Fall, A., Eichhubl, P., Bodnar, R.J., Laubach, S.E., Davis, J.S., 2015. Natural hydraulic fracturing of tight-gas sandstone reservoirs, Piceance Basin, Colorado. GSA Bulletin 127 (1/2), 61–75.

Ferrill, D.A., Smart, K.J., Cawood, A.J., Morris, A.P., 2021. The fold-thrust belt stress cycle: superposition of normal, strike-slip, and thrust faulting deformation regimes. J. Struct. Geol. 148, 104362.

Fischer, M.P., Gross, M.R., Engelder, T., Greenfield, R.J., 1995. Finite-element analysis of the stress distribution around a pressurized crack in a layered elastic medium: implications for the spacing of fluid-driven joints in bedded sedimentary rock. Tectonophysics 247, 49–64.

Forstner, S.R., Laubach, S.E., 2022. Scale-dependent fracture networks. J. Struct. Geol. 165, 104748.

Gillespie, P.A., Howard, C.B., Walsh, J.J., Watterson, J., 1993. Measurement and characterisation of spatial distributions of fractures. Tectonophysics 226, 113–141.

Gillespie, P.A., Walsh, J.J., Watterson, J., Bonson, C.G., Manzocchi, T., 2001. Scaling relationships of joint and vein arrays from the Burren, Co. Clare, Ireland. J. Struct. Geol. 23, 183–201.

Gillespie, P., 2003. Comment on "The geometric and statistical evolution of normal fault systems: an experimental study of the effects of mechanical layer thickness on scaling laws" by R.V. Ackermann, R.W. Schlische and M.O. Withjack. J. Struct. Geol. 25, 819–822.

Gomez-Rivas, E., Griera, A., 2012. Shear fractures in anisotropic ductile materials: an experimental approach. J. Struct. Geol. 34, 61–76.

Haluch, A., Rybak-Ostrowska, B., Wyglądała, M., Konon, A., Roszkowska-Remin, J., 2023. Interplay of organic matter, rock anisotropy, and horizontal shortening in bed-parallel vein development within the lower Palaeozoic shale formations from the northern part of the Caledonian Foredeep basin (Poland). Mar. Petrol. Geol. https://doi.org/10.1016/j.marpetgeo.2023.106387.

Heidbach, O., Rajabi, M., Cui, X., Fuchs, K., Müller, B., Reinecker, J., Reiter, K., Tingay, M., Wenzel, F., Xie, F., Ziegler, M.O., Zoback, M.-L., Zoback, M.D., 2018. The World Stress Map database release 2016: crustal stress pattern across scales. Tectonophysics 744, 484–498.

Hobbs, D.W., 1967. The formation of tension joints in sedimentary rocks: an explanation. Geol. Mag. 104 (6), 550–556.

Holder, J., Olson, J.E., Philip, Z., 2001. Experimental determination of subcritical crack growth parameters in sedimentary rock. Geophys. Res. Lett. 28 (4), 599–602.

Holford, S.P., Green, P.F., Hillis, R.R., Underhill, J.R., Stoker, M.S., Duddy, I.R., 2010. Multiple post-Caledonian exhumation episodes across northwest Scotland revealed by apatite fission track analysis. Journal of the Geological Society [London] 167, 675–694.

Hooker, J.N., Gale, J.F.W., Gomez, L.A., Laubach, S.E., Marrett, R., Reed, R.M., 2009. Aperture-size scaling variations in a low-strain opening-mode fracture set, Cozzette Sandstone, Colorado. J. Struct. Geol. 31, 707–718.

Hooker, J.N., Laubach, S.E., Gomez, L., Marrett, R., Eichhubl, P., Diaz-Tushman, K., Pinzon, E., 2011. Fracture size, frequency, and strain in the cambrian Eriboll Formation sandstones, NW scotland. Scot. J. Geol. 47 (1), 45–56.

Hooker, J.N., Gomez, L.A., Laubach, S.E., Gale, J.F.W., Marrett, R., 2012. Effects of diagenesis (cement precipitation) during fracture opening on fracture aperture-size scaling in carbonate rocks. In: Garland, J., Neilson, J.E., Laubach, S.E., Whidden, K.J. (Eds.), Advances in Carbonate Exploration and Reservoir Analysis, vol. 370. Geological Society [London] Special Publications, pp. 187–206.

Hooker, J.N., Laubach, S.E., Marrett, R., 2013. Fracture-aperture size—frequency, spatial distribution, and growth processes in strata-bounded and non-strata-bounded fractures, Cambrian Mesón Group, NW Argentina. J. Struct. Geol. 54, 54–71.

Hooker, J.N., Laubach, S.E., Marrett, R., 2014. A universal power-law scaling exponent for fracture apertures in sandstones. Soc. Am. Archaeol. Bull. 126 (9/10), 1340–1362.

Hooker, J.N., Katz, R.F., 2015. Vein spacing in extending, layered rock: the effect of synkinematic cementation. Am. J. Sci. 315, 557–588.

Hooker, J.N., Cartwright, J., Stephenson, B., Silver, C.R.P., Dickson, A.J., Hsieh, Y.-T., 2017a. Fluid evolution in fracturing black shales, Appalachian Basin. AAPG (Am. Assoc. Pet. Geol.) Bull. 101 (8), 1203–1238.

Hooker, J.N., Huggett, J.M., Cartwright, J., Ali Hussein, M., 2017b. Regional-scale development of opening-mode calcite veins due to silica diagenesis. G-cubed. https://doi.org/10.1002/2017GC006888.

Hooker, J.N., Laubach, S.E., Marrett, R., 2018. Microfracture spacing distributions and the evolution of fracture patterns in sandstones. J. Struct. Geol. 108, 66–79.
Hooker, J.N., Ruhl, M., Dickson, A.J., Hansen, L.N., Idiz, E., Hesselbo, S.P., Cartwright, J., 2020. Shale anisotropy and natural hydraulic fracture propagation: an example from the Jurassic (Toarcian) Posidonienschiefer, Germany. J. Geophys. Res. Solid Earth. https://doi.org/10.1029/2019JB018442.
Hooker, J.N., Fisher, D.M., 2021. How cementation and fluid flow influence slip behavior at the subduction interface. Geology 49 (9), 1074–1078.
Hooker, J.N., Marrett, R., Wang, Q., 2023. Rigorizing the use of the coefficient of variation to diagnose fracture periodicity and clustering. J. Struct. Geol. 168, 104830.
Hoyt, E.M., Hooker, J.N., 2021. Silica diagenesis and natural facturing in limestone: an example from the Ordovician of Central Pennsylvania. Mar. Petrol. Geol. 132, 105240.
Hudleston, P.J., 2015. Structures and fabrics in glacial ice: a review. J. Struct. Geol. 81, 1–27.
Ji, S., Suwatari, K., 1998. A revised model for the relationship between joint spacing and layer thickness. J. Struct. Geol. 20 (11), 1495–1508.
Ji, S., Li, L., Marcotte, D., 2021. Power-law relationship between joint spacing and bed thickness in sedimentary rocks and implications for layered rock mechanics. J. Struct. Geol. 150, 104413.
Kauffman, E.G., 1984. Paleobiogeography and evolutionary response dynamic in the cretaceous western interior Seaway of North America. In: Westermann, G.E.G. (Ed.), Jurassic-Cretaceous Biochronology and Paleogeography of North America: Geological Association of Canada Special Paper, vol. 27, pp. 273–306.
Koehn, D., Sachau, T., 2014. Two-dimensional numerical modeling of fracturing and shear band development in glacier fronts. J. Struct. Geol. 61, 133–142.
Krabbendam, M., Glasser, N.F., 2011. Glacial erosion and bedrock properties in NW Scotland: abrasion and plucking, hardness and joint spacing. Geomorphology 130, 274–383.
Lacazette, A., Engelder, T., 1992. Fluid-driven cyclic propagation of a joint in the Ithaca Siltstone, Appalachian basin, New York. In: Evans, B., Wong, T.-F. (Eds.), Fault Mechanics and Transport Properties of Rocks (U.S. Edition. Academic Press, San Diego: California, pp. 297–323.
Ladeira, F.L., Price, N.J., 1981. Relationship between fracture spacing and bed thickness. J. Struct. Geol. 3 (2), 179–183.
Lander, R.H., Larese, R.E., Bonnell, L.M., 2008. Toward more accurate quartz cement models: the importance of euhedral versus noneuhedral growth rates. AAPG (Am. Assoc. Pet. Geol.) Bull. 92 (11), 1537–1563.
Lander, R.H., Laubach, S.E., 2015. Insights into rates of fracture growth and sealing from a model for quartz cementation in fractured sandstones. GSA Bulletin 127 (3–4), 516–538.
Laubach, S.E., 1988. Subsurface fractures and their relationship to stress history in East Texas Basin sandstone. Tectonophysics 156 (1–2), 37–49.
Laubach, S.E., 1989. Paleostress directions from the preferred orientation of closed microfractures (fluid-inclusion planes) in sandstone, East Texas basin, USA. J. Struct. Geol. 11 (5), 603–611.
Laubach, S.E., Reed, R.M., Olson, J.E., Lander, R.H., Bonnell, L.M., 2004a. Coevolution of crack-seal texture and fracture porosity in sedimentary rocks: cathodoluminescence observation of regional fractures. J. Struct. Geol. 26, 967–982.
Laubach, S., Lander, R., Bonnell, L., Olson, J., Reed, R., 2004b. Opening histories of fractures in sandstone. In: Cosgrove, J.W., Engelder, T. (Eds.), The Initiation, Propagation, and Arrest of Joints and Other Fractures, vol. 231. Geological Society of London Special Publication, pp. 1–9. https://doi.org/10.1144/GSL.SP.2004.231.01.01.
Laubach, S.E., Diaz-Tushman, K., 2009. Laurentian paleostress trajectories and ephemeral fracture permeability, cambrian Eriboll Formation sandstones west of the moine thrust zone, NW scotland. Journal of the Geological Society [London] 166, 349–362.
Laubach, S.E., Olson, J.E., Gross, M.R., 2009. Mechanical and fracture stratigraphy. AAPG (Am. Assoc. Pet. Geol.) Bull. 93 (11), 1413–1426.
Laubach, S.E., Eichhubl, P., Hargrove, P., Ellis, M.A., Hooker, J.N., 2014. Fault core and damage zone fracture attributes vary along strike owing to interaction of fracture growth, quartz accumulation, and differing sandstone composition. J. Struct. Geol. 68, 207–226.
Laubach, S.E., Lander, R.H., Criscenti, L.J., Anovitz, L.M., Urai, J.L., Pollyea, R.M., Hooker, J.N., Narr, W., Evans, M.A., Kerisit, S.N., Olson, J.E., Dewers, T., Fisher, D. M., Bodnar, R.J., Evans, B., Dove, P., Bonnell, L.M., Marder, M.P., Pyrak-Nolte, L., 2019. The role of chemistry in fracture pattern development and opportunities to advance interpretations of geological materials. Rev. Geophys. 57 (3), 1065–1111.
Laubach, S.E., Zeng, L., Hooker, J.N., Wang, Q., Zhang, R., and Ren, B., submitted. Deep and ultra-deep basin brittle deformation with focus on China. J. Struct. Geol..
Lee, H.P., Olson, J.E., Holder, J., Gale, J.F.W., Myers, R.D., 2014. The interaction of propagating opening mode fractures with preexisting discontinuities in shale. J. Geophys. Res. Solid Earth 120, 169–181. https://doi.org/10.1002/2014JB011358.
Li, B., Robinson, L., 2018. Natural Fractures, Fracture Facies, and Their Applications in the Well Completion - Case Studies from the Permian Wolfcamp Formation, Midland Basin. SPE/AAPG/SEG Unconventional Resources Technology Conference, West Texas, USA. https://doi.org/10.15530/URTEC-2018-2902102. Houston, Texas, USA, paper URTEC-2902102-MS.
Li, J.Z., Laubach, S.E., Gale, J.F.W., Marrett, R., 2018. Quantifying opening-mode fracture spatial organization in horizontal wellbore image logs, core and outcrop: application to Upper Cretaceous Frontier Formation tight gas sandstones, USA. J. Struct. Geol. 108, 137–156.
Liu, Z., Zhang, L., Liu, G.R., Li, W., Li, S., Wang, F., Ma, Y., Li, H., Zhang, H., Han, L., 2020. Material constituents and mechanical properties and macro-micro-failure modes of tight gas reservoirs. Energy Explor. Exploit. 38 (6), 2631–2648.
Lorenz, J.C., Finley, S.J., 1991. Regional fractures II: fracturing of Mesaverde reservoirs in the Piceance basin, Colorado. AAPG (Am. Assoc. Pet. Geol.) Bull. 75 (11), 1738–1757.
Major, J.R., Eichhubl, P., Dewers, T.A., Olson, J.E., 2018. Effect of CO_2-brine-rock interaction on fracture mechanical properties of CO_2 reservoirs and seals. Earth Planet Sci. Lett. 499, 37–47.
Manzocchi, T., 2002. The connectivity of two-dimensional networks of spatially correlated fractures. Water Resoures Research 38 (9). https://doi.org/10.1029/2000WR000180.
Marrett, R., Ortega, O.J., Kelsey, C.M., 1999. Extent of power-law scaling for natural fractures in rock. Geology 27 (9), 799–802.
Marrett, R., Gale, J.F.W., Gómez, L.A., Laubach, S.E., 2018. Correlation analysis of fracture arrangement in space. J. Struct. Geol. 108, 16–33.
Meredith, P.G., Atkinson, B.K., 1985. Fracture toughness and subcritical crack growth during high-temperature tensile deformation of Westerly granite and Black gabbro. Phys. Earth Planet. In. 39 (1), 33–51.
Monsees, A.C., Blebricher, S.F., Busch, B., Feinendegen, M., Ziegler, M., Hilgers, C., 2021. Coupling diagenetic alterations and mechanical properties of Lower Permian siliciclastic sandstones: a pilot study. Environ. Earth Sci. 80, 141.
Mount, V.S., 2014. Structural style of the Appalachian Plateau fold belt, north-central Pennsylvania. J. Struct. Geol. 69, 284–303.
Myers, R., Aydin, A., 2004. The evolution of faults formed by shearing across joint zones in sandstone. J. Struct. Geol. 26, 947–966.
Nuccio, V.F., Roberts, L.N.R., 2003. Thermal maturity and oil and gas generation history of petroleum systems in the Uinta-Piceance province, Utah and Colorado, Chapter 4. In: Petroleum Systems and Geologic Assessment of Oil and Gas in the Uinta-Piceance Province, Utah and Colorado: U.S. Geological Survey Digital Data Series DDS-69-B CD-ROM. USGS Uinta-Piceance Assessment Team, p. 39.
Olson, J., Pollard, D.D., 1989. Inferring paleostresses from natural fracture patterns: a new method. Geology 17, 345–348.
Olson, J.E., 1993. Joint pattern development: effects of subcritical crack growth and mechanical crack interaction. J. Geophys. Res. 98 (B7), 12251–12265.
Olson, J.E., 2003. Sublinear scaling of fracture aperture versus length: an exception or the rule? J. Geophys. Res. 108 (B9), 2413. https://doi.org/10.1029/2001JB000419.
Olson, J.E., 2004. Predicting fracture swarms – the influence of subcritical crack growth and the crack-tip process zone on joint spacing in rock. In: Cosgrove, J.W., Engelder, T. (Eds.), The Initiation, Propagation, and Arrest of Joints and Other Fractures, vol. 231. Geological Society of London Special Publication, pp. 73–87.
Olson, J.E., Laubach, S.E., Lander, R.H., 2009. Natural fracture characterization in tight gas sandstones: integrating mechanics and diagenesis. AAPG (Am. Assoc. Pet. Geol.) Bull. 93 (11), 1535–1549.
Onasch, C.M., 1990. Microfractures and their role in deformation of a quartz arenite from the central Appalachian foreland. J. Struct. Geol. 12 (7), 883–894.
Ortega, O.J., Gale, J.F.W., Marrett, R.A., 2010. Quantifying diagenetic and stratigraphic controls on fracture intensity in platform carbonates. J. Struct. Geol. 32, 1943–1959.
Peach, B.N., Horne, J., Gunn, W., Clough, C.T., Hinxman, L.W., Teall, J.J., 1907. The Geological Structure of the Northwest Highlands of Scotland. Memoirs of the Geological Survey, U.K.
Peacock, D.C.P., Sanderson, D.J., 1992. Effects of layering and anisotropy on fault geometry. Journal of the Geological Society of London 149, 793–802.
Petit, J.-P., Chemenda, A.I., Minisini, D., Richard, P., Bergman, S.C., Gross, M., 2022. When do fractures initiate during the geological history of a sedimentary basin? Test case of a loading-fracturing path methodology. J. Struct. Geol. https://doi.org/10.1016/j.jsg.2022.104683.
Pollard, D.D., Aydin, A., 1988. Progress in understanding jointing over the past century. GSA Bulletin 100, 1181–1204.
Price, N.J., 1966. Fault and Joint Development in Brittle and Semi-brittle Rock. Pergamon Press, Oxford, p. 176.
Qin, S., Wang, R., Shi, W., Liu, K., Zhang, W., Xu, X., Qi, R., Yi, Z., 2022. Diverse effects of intragranular fractures on reservoir properties, diagenesis, and gas migration: insight from Permian tight sandstone in the Hangjinqi area, north Ordos Basin. Mar. Petrol. Geol. 137, 105526.
Ramsay, J.G., 1980. The crack-seal mechanism of rock deformation. Nature 284, 135–139.
Rinehart, A.J., Dewers, T., Broome, S.T., Eichhubl, P., 2016. Effects of CO_2 on mechanical variability and constitutive behavior of the lower tuscaloosa formation, cranfield injection site, USA. Int. J. Greenh. Gas Control 53, 305–318.
Romano, C.R., Williams, R.T., 2022. Evolution of fault-zone hydromechanical properties in response to different cementation processes. Lithosphere 2022, 1069843.
Saïag, J., Brigaud, B., Portier, É., Desaubliaux, G., Bucherie, A., Miska, S., Pagel, M., 2016. Sedimentological control on the diagenesis and reservoir quality of tidal sandstones of the upper cape hay formation (permian, Bonaparte basin, Australia). Mar. Petrol. Geol. 77, 597–624.
Sanderson, D.J., Peacock, D.C.P., Nixon, C., Rotevatn, A., 2018. Graph theory and the analysis of fracture networks. J. Struct. Geol. https://doi.org/10.1016/j.jsg.2018.04.011.
Savalli, L., Engelder, T., 2005. Mechanisms controlling rupture shape during subcritical growth of joints in layered rocks. GSA Bulletin 117 (3/4), 436–449. https://doi.org/10.1130/B25368.1.
Schöpfer, M.P.J., Arslan, A., Walsh, J.J., Childs, C., 2011. Reconciliation of contrasting theories for fracture spacing in layered rocks. J. Struct. Geol. 33, 551–565.
Secor Jr., D.T., 1965. Role of fluid pressure in jointing. Am. J. Sci. 263, 633–646.

Späth, M., Urai, J.L., Nestler, B., 2022. Incomplete crack sealing causes localization of fracturing in hydrothermal quartz veins. Geophys. Res. Lett. 49, e2022GL098643.
Srivastava, D.C., Engelder, T., 1990. Crack-propagation sequence and pore-fluid conditions during fault-bend folding in the Appalachian Valley and Ridge, central Pennsylvania. GSA Bulletin 102, 116–128.
Tan, T., Johnston, T., Engelder, T., 2014. The concept of joint saturation and its application. AAPG (Am. Assoc. Pet. Geol.) Bull. 98 (11), 2347–2364.
Trewin, N.H., Rollin, K.E., 2002. Geologic history and structure of Scotland. In: Trewin, N.H. (Ed.), The Geology of Scotland. The Geological Society, London, pp. 1–25. https://doi.org/10.1144/GOS4P.
Urai, J.L., Williams, P.F., van Roermund, H.L.M., 1991. Kinematics of crystal growth in syntectonic fibrous veins. J. Struct. Geol. 13 (7), 823–836.
Vass, A., Koehn, D., Toussaint, R., Ghani, I., Piazolo, S., 2014. The importance of fracture-healing on the deformation of fluid-filled layered systems. J. Struct. Geol. 67, 94–106.
Virgo, S., Abe, S., Urai, J.L., 2014. The evolution of crack seal vein and fracture networks in an evolving stress field: insights from discrete element models of fracture sealing. J. Geophys. Res. Solid Earth 119, 8708–8727.
Walderhaug, O., 1996. Kinetic modeling of quartz cementation and porosity loss in deeply buried sandstone reservoirs. AAPG (Am. Assoc. Pet. Geol.) Bull. 80 (5), 731–745.
Wilkins, S., Mount, V., Mahon, K., Perry, A., Koenig, J., 2014. Characterization and development of subsurface factures observed in the Marcellus Formation, Appalachian Plateau, north-central Pennsylvania. AAPG (Am. Assoc. Pet. Geol.) Bull. 98 (11), 2301–2345.
Wilson, R.W., Holdsworth, R.E., Wild, L.E., McCaffrey, K.J.W., England, R.W., Imber, J., Strachan, R.A., 2010. Basement-influenced rifting and basin development: a reappraisal of post-Caledonian faulting patterns from the North Coast Transfer Zone, Scotland. In: Law, R.D., Butler, R.W.H., Holdsworth, R.E., Krabbendam, M., Strachan, R.A. (Eds.), Continental Tectonics and Mountain Building: the Legacy of Peach and Horne, vol. 335. Geological Society (London) Special Publications, pp. 795–826.